Title

Multiscale robust topology for fiber composites with multiscale material uncertainty propagation

Permalink

https://escholarship.org/uc/item/7rj4n42z

Author

Diaz Flores Caminero, Alvaro

Publication Date

2024

Peer reviewed|Thesis/dissertation

UNIVERSITY OF CALIFORNIA SAN DIEGO

Multiscale robust topology optimization for fiber composites with multiscale material uncertainty propagation

A thesis submitted in partial satisfaction of the
requirements for the degree Master of Science

in

Structural Engineering

by

Alvaro Diaz Flores Caminero

Committee in charge:

Professor Hyunsun Alicia Kim, Chair
Professor Mayank Chadha
Professor Hyonny Kim

2024

The thesis of Alvaro Diaz Flores Caminero is approved, and it is acceptable in quality and form for publication on microfilm and electronically.

University of California San Diego

2024

DEDICATION

To my parents for their endless patience and unwavering support throughout this journey. Your encouragement has been the cornerstone of my perseverance.

To Hwee Ru, thank you for your constant support and understanding and for the stress-relieving massages that helped me recharge during challenging times. Your care and love have been truly invaluable. As of today, you are a fantastic girlfriend, in the future I don't know.

To me for putting in all the hard work. For relentlessly finding solutions to problems and for providing incredible and undervalued work.

To all of you, thank you for being part of this journey, I couldn't have done it without you.

EPIGRAPH

<u>And you may ask yourself,</u>
<u>Well, how did I get here?</u>

Talking heads

TABLE OF CONTENTS

LIST OF FIGURES

LIST OF TABLES

ACKNOWLEDGEMENTS

I extend my heartfelt thanks to Alex Guibert for your limitless technical advice and guidance and to Hussein for stepping in during my toughest moments, pulling me out of exhaustion and doubt, and teaching me how to sell a story.

To Douglas and Carolina, thank you for introducing me to the climbing group and giving me a new avenue to find balance and perspective. To Noza, thank you for the invigorating Navy Seals workouts, which pushed me to stay resilient and focused.

Lastly, I want to express my appreciation to the M2DO group for fostering a workplace that feels truly worth belonging to. Your camaraderie and support made this journey not only manageable but also enjoyable.

Chapter 1, in part is currently being prepared for submission for publication of the material. Diaz-Flores Caminero, Alvaro; Ismail, Hussein; Chaudhuri, Anirban; Kim, H. Alicia. The thesis author was the primary investigator and author of this material.

Chapter 2, in part is currently being prepared for submission for publication of the material. Diaz-Flores Caminero, Alvaro; Ismail, Hussein; Chaudhuri, Anirban; Kim, H. Alicia. The thesis author was the primary investigator and author of this material.

Chapter 3, in part is currently being prepared for submission for publication of the material. Diaz-Flores Caminero, Alvaro; Ismail, Hussein; Chaudhuri, Anirban; Kim, H. Alicia. The thesis author was the primary investigator and author of this material.

Chapter 4, in part is currently being prepared for submission for publication of the material. Diaz-Flores Caminero, Alvaro; Ismail, Hussein; Chaudhuri, Anirban; Kim, H. Alicia. The thesis author was the primary investigator and author of this material.

Chapter 5, in part is currently being prepared for submission for publication of the material. Diaz-Flores Caminero, Alvaro; Ismail, Hussein; Chaudhuri, Anirban; Kim, H. Alicia. The thesis author was the primary investigator and author of this material.

ABSTRACT OF THE THESIS

Multiscale robust topology optimization for fiber composites with multiscale material uncertainty propagation

by

Alvaro Diaz Flores Caminero

Master of Science in Structural Engineering

University of California San Diego, 2024

Professor Hyunsun Alicia Kim, Chair

A multiscale multi-fidelity robust topology Optimization (MFRTO) is proposed to design continuous fiber-reinforced composites (CFRC) components minimizing the structural compliance mean and variance subjected to material uncertainties within a prescribed volume constraint. The topology optimization problem employs the level set method, where the fiber orientation is continuously updated following principle stress approach. At the macro level, multi fidelity

Monte Carlo (MFMC) is used to compute the mean and variance of the structural compliance utilizing a density filter creating lower mesh-related fidelity models from the highest fidelity models. Likewise, the mean and variance of the macroscopic elastic properties of a unidirectional fiber-reinforced composite are computed via different fidelity numerical homogenization approaches, specifically the generalized method of cells (GMC) and High-Fidelity GMC (HFGMC). Numerical simulations are performed to validate the proposed algorithm, showcasing peculiar features of the achieved optimal solutions with respect to the topology found in the case of deterministic materials. The paper also discusses the computational efficiency of the approach, particularly the speed-up achieved compared to the traditional Monte Carlo method.

Keywords: Multi-Scale Robust Topology Optimization, Fiber-Reinforced Composites, Material Uncertainty, Multi-fidelity Monte Carlo.

Chapter 1

Introduction

In this chapter, we tackle the current state of the art in topology optimization of continuous fiber-reinforced composites under uncertainty, as well as explain the challenges that need to be addressed. For that purpose, we did a literature review.

Composite materials, particularly continuous fiber-reinforced composites, have gained significant attention in engineering applications due to their high strength-to-weight ratios and customizable properties. However, the complexity of their microstructures poses challenges in design and analysis. Since the microscopic fiber patterns are significantly smaller in scale relative to the overall dimensions of macro-scale components, homogenization techniques can be employed to derive effective macroscopic material properties. This approach averages out the complex microstructural details, resulting in simplified yet accurate material characteristics that reflect the overall behavior of the composite material.

Building on this concept, Aboudi [1] provided a review of homogenization techniques, namely the Generalized Method of Cells (GMC) and its enhanced version, the High-Fidelity Generalized Method of Cells (HFGMC). Those methods have been widely used for their ability to capture microstructural details and predict the macroscopic behavior of composites. The GMC method provides a semi-analytical approach to homogenization by modeling the composite as an assemblage of repeating unit cells, allowing for efficient computation of effective properties. The HFGMC extends this method by incorporating higher-order displacement fields within the unit cells, leading to improved accuracy in capturing stress and strain distributions.

Numerical methods such as finite element-based homogenization have also been employed to model the complex behavior of fiber composites. Kouznetsova et al. [34] introduced a gradient-enhanced computational homogenization method that models microstructural size effects within a nonlinear framework. Andreassen [5] provided an educational description of numerical homogenization, presenting an efficient method to determine the effective macroscopic properties of periodic composite materials, such as the elasticity tensor, using a simple Matlab implementation that can be extended to multiple materials, conductivity, thermal expansion, and fluid permeability with flexibility in 2D periodic unit cell shapes. Furthermore, Bruggi el al. [10] applied the integration of homogenization techniques with multi-scale topology optimization enabling the design of composite materials with optimized structural performance incorporating uncertainty in loading amplitude. This approach allows for the simultaneous optimization of both the macroscopic structure and the microscopic material layout, leading to advanced composite designs with tailored properties.

Integrating optimal fiber orientation and external shape into a single numerical process can be achieved through topology optimization which has proven to be an effective and efficient method for addressing this design challenge, as highlighted in recent review [54]. The classical topology optimization problem looks for the optimal distribution of a given amount of material inside a prescribed domain, in order to optimize the mechanical response of the body to a given load. Multi-scale topology optimisation approach utilizes the separation of scales, where numerical homogenization is applied to model the microstructure—whether at the micro- or meso-scale—by employing equivalent material properties at the macro-scale [27, 41].

Most topology optimization work has been conducted for isotropic materials, where properties are uniform in all directions, simplifying the optimization process. However, extending topology optimization to anisotropic materials, such as composites, introduces additional challenges and complexities due to the directional dependence of material properties, including accurately modeling the anisotropic behavior within the optimization framework, ensuring manufacturability of the optimized designs, and managing increased computational demands. To effectively align the anisotropy of microstructures to stress directions, it is possible to release the rotational freedom in the unit cell, as pioneered by Bendsøe and Kikuchi [7]. Groen [26] developed a method that allows the dimensions of the members in different principal directions of the cubic unit cell to vary independently. By also permitting the unit cells to rotate, these methods are able to generate lattices with orthotropic properties that are truly adapted to the macroscale loads. In fiber composite materials, fiber orientation can effectively tailor structural performance in stress concentration problems [46], stiffness [39], buckling [6], and natural frequency [56]. Ghandi et al. [23] classified in his review different parameterizing techniques for anisotropic materials' topology optimization including the continuous parameterization of fiber orientation (CFO), where the design uses the orientation angle itself as the design variable.

CFO approaches trace back to when Pedersen [42] derived an analytical expression to optimize the fiber angle based on the principal strain directions—the strain-based method. Soon after, Suzuki and Kikuchi [47] proposed the stress-based method, which, despite their similarity, produces a slightly stiffer structure than the strain method due to strong couplings among the orientation variables in the strain-based method [15]. Later, Gea and Luo [24] demonstrated that the fiber orientation coincides with the principal stress/strain fields for relatively weak shear and some strong shear types of anisotropic materials, avoiding the non-uniqueness. Heitkamp et al. [29], presents a method for improving the mechanical properties of additively manufactured parts by embedding continuous fibers along principal stress trajectories. This approach, as compared to traditional unidirectional fiber alignment, resulted in a tensile strength increase by a factor of 3 and a flexural strength improvement by a factor of 1.9, demonstrating the effectiveness of stress-oriented fiber placement. Zheng et al. [44], introduces a method for optimizing continuous fiber-reinforced composites (CFRCs) that accounts for the differing moduli in tension and compression. The method incorporates the tension/compression bi-modulus orthotropic property using a weighted compliance matrix (WCM) material model and optimizes fiber orientation by aligning it with the principal stress directions. Matteo et al. [11] proposed a procedure to achieve the optimal layout of fiber-reinforced polymer (FRP) reinforcements for masonry structures based on a topology optimization approach, where the layout of the reinforcement is completely free to rotate independently. The optimal orientation of the fibers found to be close, but not identical, to the direction of the tensile principal stresses of the underlying panel, which can be conveniently implemented as a starting guess for the fiber orientation in the optimization procedure.

Desai et al. [19] used topological derivatives to obtain the distribution of fiber, matrix, and voids along with the fiber orientation, which they then post-process to achieve evenly spaced fiber trajectories suitable for manufacturing. Jantos et al. [32] applied a thermodynamics-based orientation approach for anisotropic materials to classical topology optimization problems, enhancing the method through a filtering technique to control fiber smoothness. Li et al. [37] proposed a one-scale topology optimization framework with fiber composites' orientation and morphology optimization, including fiber volume fraction, spacing, and thickness. Boddeti et al. [8] introduced a design-to-manufacture multiscale workflow for composite materials, where fiber and matrix properties undergo homogenization, and fiber orientation follows a continuous parameterization approach. Wang et al. [52] developed a new algorithm for fiber placement—Stress Vector Tracing algorithm—to create load-dependent and continuous fiber paths. Fernandes et al. [22] demonstrated 3D printing fabrication feasibility and testing of a carbon fiber-reinforced composite (CFRC) structure with topology optimization and optimal fiber orientation. Haichao et al. [4] introduced a multi-fidelity approach to fuse models of varying fidelity and optimize fiber orientation and topology in buckling problems using a genetic algorithm.

In the past decade, there has been a significant increase in the number of works addressing topology optimization under uncertainties. These publications are generally classified based on the specific object of topology optimization, the numerical procedures employed, and the sources of uncertainty (e.g., loading, geometry, stiffness, production tolerance, material properties). Tootkaboni et al. [50] highlighted that, under real-world conditions, many of the terms in the optimization problem, including applied loads, and the stiffness of the structure, may involve some degree of uncertainty. Schuëller [45] presented a review on some of the most relevant developments in the field of optimization under uncertainty. One prominent approach is Reliability-Based Design Optimization (RBDO), which seeks to minimize the probability of failure for a given objective by either reducing the area under the probability density function that falls outside the success boundaries or by shifting the mean value further away from these boundaries. As highlighted by Tauzowski [48], reliability analysis itself is an optimization procedure, therefore, applying reliability as a constraint in topology optimization becomes a complex problem referred to as nested optimization. More examples of Reliability Based Topology Optimization include works by Kharmanda et al. [33], Wang et al. [51, 53], and Zeshang et al. [38].

Alternatively, Robust Design Optimization (RDO) focuses on minimizing the impact of stochastic variability on the mean design by integrating higher-order statistics, such as variance, into the optimization process. The robust optimization procedure typically involves two phases: an initial deterministic optimization aimed at performance enhancement, followed by a sensitivity analysis that accounts for uncertainties. Dunning et al. [20, 21] introduced a robust structural topology optimization method that is both efficient and precise, aiming to minimize the expected compliance while accounting for uncertainties in both the magnitude and direction of applied loads.

Deng et al. [18] introduced a multiscale topology optimization approach for porous materials under Gaussian random field loading uncertainties. However, when the random field is non-Gaussian, one must use a Monte Carlo method to compute a fourth-order statistical moment, making it computationally intensive. More examples of robust topology optimization under loading uncertainty include works by Cai et al. [13], Yanan et al. [55], and Cai et al. [12]. Sheng et al. [16] proposed a non-intrusive solution using Monte Carlo simulations combined with a Kriging model to accelerate computation and optimize the topology and fiber orientation of fiber-reinforced composite structures under loading uncertainty.

Despite advancements in uncertainty quantification methods, previous research has predominantly concentrated on uncertainties associated with structural design parameters, such as applied loads, while comparatively less emphasis has been placed on uncertainties related to material properties. This distinction is critical, as material uncertainty can significantly influence the performance and reliability of composite structures.

Agrawal et al. [3] presented a robust topology optimization (RTO) method to address material uncertainties in negative Poisson ratio metamaterials, achieving significantly more stable designs compared to deterministic optimization. Hamdia et al. [28] proposed a multilevel Monte Carlo method to speed up computation in topology optimization of flexoelectric composites with material uncertainty. Kumar et al. [35] introduced an efficient uncertainty quantification and global sensitivity analysis method for composite applications through sparse polynomial chaos expansion enhanced with Latin hypercube sampling. In a subsequent publication, Kumar et al. [36] expanded this research to include multi-scale uncertainties, such as laminate orientation and thickness, using Sparse Polynomial Chaos Expansion (SPCE) and gradient-free genetic algorithm NSGA II to optimize stiffness and cost under a 99.5% mass constraint reliability. Thillaithevan et al. [49] demonstrated a robust optimization methodology for multivariable parameterized lattice microstructures by introducing material uncertainties at the microscale through uncertain perturbations to the lattice truss radii. Zheng et al. [57] explored the effects of material uncertainty, specifically elastic modulus and Poisson's ratio uncertainties, on the performance and topology optimization of multi-material structures, using non-intrusive polynomial chaos expansion. Hyun et al. [30] a robust topology optimization method for isotropic materials using density-based topology optimization, addressing material uncertainty through the multifidelity Monte Carlo (MFMC) approach. The method integrates low-cost, low-fidelity models with a high-fidelity model to reduce the computational burden typically associated with traditional Monte Carlo simulations. The proposed methodology demonstrates efficient resource allocation and achieves a significant computational speed-up while preserving accuracy, as confirmed by numerical examples.

In summary, current approaches in multiscale topology optimization for fiber-reinforced composites have advanced the integration of optimal fiber orientation and structural topology, using homogenization techniques to handle microstructural complexities. Despite advancements in modeling anisotropic behaviors and accounting for uncertainties in loading and geometry, the incorporation of material uncertainties—-especially in fiber and matrix properties–remains underdeveloped. Current approaches utilize computationally intensive Monte Carlo (MC) simulations for uncertainty quantification, which, while accurate, are often impractical due to high computational costs. To address this, other methods have been developed that aim to improve efficiency, sometimes at the expense of accuracy.

We propose a multiscale framework that can guarantee an upper bound for the mean-squared error of the propagated mechanical properties and the objective function, achieving a maximum combined speedup of 298 times compared to Monte-Carlo simulation. In addition, we apply this method to optimize the topology and fiber orientation of a CFRC structure using the level-set method.

Chapter 1, in part is currently being prepared for submission for publication of the material. Diaz-Flores Caminero, Alvaro; Ismail, Hussein; Chadhuri, Anirban; Kim, H. Alicia. The thesis author was the primary investigator and author of this material.

Chapter 2

Formulation

Consider a Cartesian coordinate system $Oz_1z_2z_3$, where a three-dimensional body composed of a linear elastic material occupies the region Ω. The stress and strain components, denoted by σ_{ij} and ε_{ij}, respectively, are related through the material's constitutive law, which can be expressed as:

$$\sigma_{ij} = C_{ijkl}\varepsilon_{kl} \tag{2.1}$$

where C_{ijkl} is the fourth-order elasticity tensor, capturing the anisotropic response of the material. Under the assumption of plane stress, the elasticity tensor $\mathbf{C}$ simplifies as out-of-plane stress σ_{33} is zero. The in-plane elasticity tensor is given by:

$$\mathbf{C} = \begin{bmatrix} C_{11} & C_{12} & C_{16} \\ C_{12} & C_{22} & C_{26} \\ C_{61} & C_{62} & C_{66} \end{bmatrix} \tag{2.2}$$

Let θ be the angle between the global X-axis and the fiber direction. To incorporate this fiber orientation, the elasticity tensor in the global coordinate system can be obtained by rotating the local elasticity tensor using a rotation matrix $\mathbf{T}(\theta)$. The transformed elasticity tensor in the global coordinate system is given by:

For fiber-reinforced composite materials, the orientation of the fibers significantly influences the material's stiffness. Let θ denote the angle between the global X-axis and the fiber direction. To account for this fiber orientation, the elasticity tensor in the global coordinate system is derived from the local coordinate system using a rotation matrix $\mathbf{T}(\theta)$. The transformed elasticity tensor in the global system is given by:

$$\mathbf{C}(\theta) = \mathbf{T}(\theta)\mathbf{C}\mathbf{T}^T(\theta) \tag{2.3}$$

2.1 Multi-scale Level set Topology Optimization: Deterministic Case

2.1.1 Preliminaries

A classical problem in topology optimization is to determine the optimal material distribution within a structure that maximizes its stiffness. In other words, the goal is to find the optimal distribution of material within a given domain Ω, such that the structural compliance is minimized while satisfying a volume fraction constraint.

In the context of multi-scale topology optimization for fiber composite, the boundaries evolve at the macro scale using the level set method, where material regions are tracked by a level set function $\phi(\mathbf{x})$ at point $x \in \Omega$. Successively, fiber orientation at the micro-scale is found to minimize the strain energy through a sub-optimization routine described in section 2.1.3.

The homogenized elasticity tensor of the fiber composite is derived through a micromechanical analysis technique within the framework of the Method Of Cells (MOC), which provides the overall behavior of a multiphase material by taking into account the response of the individual constituents, their volume fractions, and the detailed interaction between the phases. In this work, the adopted method is the most recent generalization of Method Of Cells, referred to as the High Fidelity Generalized Method Of Cells (HFGMC). This method can provide the overall behavior of periodic multiphase materials of various types, including thermoelastic, viscoelastic, thermo-inelastic, and electromagnetothermoelastic materials [1].

The level set function defines the material layout within the domain Ω, where the sign of $\phi(\mathbf{x})$ differentiates between solid material and void regions. The level set function is defined as:

$$\phi(\mathbf{x}) = \begin{cases} 0 & \text{on the material boundary,} \\ < 0 & \text{inside the material (solid region),} \\ > 0 & \text{outside the material (void region).} \end{cases} \tag{2.4}$$

Ersatz material model is used to apply the level set field on a fixed analysis mesh where each element's material density is interpolated based on the area fraction of the element that lies within the solid region. For elements fully within the solid region ($\phi(\mathbf{x}) < 0$), the volume fraction $\rho(\mathbf{x})$ is set to 1, while for elements fully in the void region ($\phi(\mathbf{x}) > 0$), $\rho(\mathbf{x})$ is close to zero. For elements intersecting the boundary ($\phi(\mathbf{x}) = 0$), an intermediate volume fraction is computed, [40]. This volume fraction $\rho(\mathbf{x})$ is then used to define the elasticity tensor at any point in the domain supporting partial densities and enabling smooth transitions across boundaries:

$$\mathbf{C}(\theta, \phi(x)) = \mathbf{C}_{min} + \rho(\phi(x))(\mathbf{C}(\theta)_0 - \mathbf{C}_{min}), \tag{2.5}$$

where:

- $\mathbf{C}_{\text{min}}$ is the elasticity tensor in void regions,
- $\mathbf{C}(\theta)_0$ is the homogenized elasticity tensor for fully solid material in orientation θ,
- $\rho(\mathbf{x})$ interpolates material properties based on $\phi(\mathbf{x})$.

2.1.2 Optimization problem Formulation

The minimum compliance volume constrained multi-scale topology optimization problem for fiber composite accounting for fiber orientation can now be formulated as:

$$
\begin{cases}
\min\limits_{\phi} \quad J(\phi,\theta) = \displaystyle\int_{\Omega} \mathbf{u}^T \mathbf{K}(\rho(x),\theta)\mathbf{u}\, d\Omega & \text{(2.6a)} \\
\text{subject to:} \quad \displaystyle\int_{\Omega} \rho(x)\, d\Omega \leq V^*, & \text{(2.6b)}
\end{cases}
$$

where $J(\rho,\theta)$ is the compliance (or strain energy), $\mathbf{K}(\rho,\theta)$ is the global stiffness matrix dependent on the material distribution and orientation θ, and V^* is the volume constraint.

The level set boundary evolves over time according to the Hamilton–Jacobi equation, which tracks the boundary motion:

$$
\frac{\partial \phi(\mathbf{x},t)}{\partial t} + v(\mathbf{x},t)|\nabla \phi(\mathbf{x},t)| = 0, \tag{2.7}
$$

where $v(\mathbf{x},t)$ is the normal velocity field, computed from the sensitivity of the objective function guiding the boundary toward optimal configurations under prescribed constraints.

2.1.3 Orientation update

Material properties of composite materials reinforced with fibers can be improved for a specific application tailoring fiber orientation [17]. Gibiansky and Cherkaev [25] and Suzuki and Kikuchi [47] showed that the optimal orientation of orthotropic material could be where it is co-aligned along its major principal stress direction. Gea in his paper [24], showed that optimal orientation of both shear “weak” and some shear “strong” orthotropic materials may coincide with the major principal stress direction in the stress-based method.

In this work, an iterative procedure was implemented to achieved coaxiality between the principal stress and strain tensors in a two-dimensional (2D) framework, aiming to achieve an optimal fiber orientation that minimize the strain energy. The process starts with an initial stress tensor $\boldsymbol{\sigma}^{(0)}$ and an elasticity tensor $\mathbf{C}^{(0)}$, alongside a known strain tensor $\boldsymbol{\varepsilon}$ derived from the material’s deformation state. At each iteration n, the eigenvalues $\lambda_i^{(n)}$ and corresponding eigenvectors $\mathbf{v}_i^{(n)}$ of the stress tensor $\boldsymbol{\sigma}^{(n)}$ were computed by solving the eigenvalue problem:

$$\boldsymbol{\sigma}^{(n)}\mathbf{V}^{(n)} = \mathbf{V}^{(n)}\boldsymbol{\Lambda}^{(n)}, \tag{2.8}$$

where

$$\mathbf{V}^{(n)} = \begin{bmatrix} \mathbf{v}_1^{(n)} & \mathbf{v}_2^{(n)} \end{bmatrix} \quad \text{and} \quad \boldsymbol{\Lambda}^{(n)} = \begin{bmatrix} \lambda_1^{(n)} & 0 \\ 0 & \lambda_2^{(n)} \end{bmatrix}. \tag{2.9}$$

The eigenvector $\mathbf{v}_{\max}^{(n)}$ associated with the maximum absolute principal stress $\lambda_{\max}^{(n)} = \max\left(\left|\lambda_1^{(n)}\right|, \left|\lambda_2^{(n)}\right|\right)$ was identified to determine the principal direction of highest stress magnitude. The fiber orientation $\theta^{(n+1)}$ is then updated to align with $\mathbf{v}_{\max}^{(n)}$:

$$\theta^{(n+1)} = \operatorname{arctan2}\left(v_{\max,y}^{(n)},\, v_{\max,x}^{(n)}\right). \tag{2.10}$$

A fourth-order rotation matrix, transformed to a two-dimensional one, $\mathbf{T}^{(n)}$, by means of [9], was subsequently constructed to align the elasticity tensor with $\mathbf{v}_{\max}^{(n)}$, facilitating the transformation of the elasticity tensor as follows:

$$\mathbf{C}^{(n+1)} = \mathbf{T}^{(n+1)}\mathbf{C}^{(n)}\mathbf{T}^{(n+1)\top}. \tag{2.11}$$

This rotated elasticity tensor $\mathbf{C}^{(n+1)}$ was then utilized to compute the updated stress tensor $\boldsymbol{\sigma}^{(n+1)}$ through the constitutive relation:

$$\boldsymbol{\sigma}^{(n+1)} = \mathbf{C}^{(n+1)} : \boldsymbol{\varepsilon}. \tag{2.12}$$

The principal stresses and their corresponding directions were recalculated for $\boldsymbol{\sigma}^{(n+1)}$, and the alignment process was repeated iteratively. The convergence of the iterative procedure is evaluated by computing the difference between the fiber orientations of successive iterations:

$$\Delta\theta^{(n)} = \left|\theta^{(n)} - \theta^{(n-1)}\right| < \varepsilon. \tag{2.13}$$

When $\Delta\theta^{(n)}$ falls below a predetermined tolerance ε, the iterative process is considered to have converged.

2.2 Multi-scale Level set Topology Optimization: Robust Case

In this work, material uncertainties (UQ) at the micro-scale are considered. The uncertainty quantification of the homogenized elastic tensor entries, of the composite material, is derived by considering the uncertainties in one or more quantities of interest, specifically the material properties, of the fibers, the matrix, or both. Solving the UQ problem involves computing the statistical moments of each QOI, specifically the mean and the variance of uncertain elastic tensor entries. Monte Carlo simulation serves as the most general approach for this analysis leading to a high uncertainty estimation accuracy while considering a large number of high-fidelity samples.

Considering the multi-scale topology optimization for fiber composite problems, uncertainty quantification occurs at both the microscale and macroscale levels. At the microscale, the UQ problem is addressed by determining the statistical moments for each homogenized element of the constitutive tensor, for different fiber orientations. Subsequently, the design boundaries are updated based on the sensitivity analysis of these statistical moments of structural compliance. Employing Monte Carlo simulation with high-fidelity models for UQ in this multi-scale procedure is computationally expensive. Jaeyub et al. [30] proposed an efficient procedure for minimum compliance volume-constrained robust topology optimization accounting for material single using multi-fidelity Monte Carlo (MFMC).

In this work, an updated version of MFMC is developed to account for single or multiple QOI. MFMC works as a sub-optimization routine, taking advantage of low-fidelity models and allocating tailored computational resources for model, reducing the computational cost without compromising the accuracy of the UQ compared to high fidelity Monte Carlo analysis. [30]

2.2.1 Optimization problem formulation

By accounting for the mirco scale uncertainty and deriving the mean and the variance of the homogenized material properties, the deterministic topology optimization framework proposed in section 2.1 is extended to account for these uncertainties. Consequently, a robust topology optimization formulation is formulated as follows:

$$
\begin{cases}
\min\limits_{\phi} \quad J(\phi, Z) = \eta \cdot \ln\left(\mathbb{E}\left[f(\rho, Z)\right]\right) + (1-\eta) \cdot \ln\left(\sqrt{\mathrm{Var}\left[f(\rho, Z)\right]}\right) & \text{(2.14a)} \\
\text{subject to:} \quad \int_{\Omega} \rho(x)\, d\Omega \leq V^*, & \text{(2.14b)}
\end{cases}
$$

where the objective function $J(\rho, Z)$ is a weighted combination of the expected value of the structural compliance $\mathbb{E}[f(\rho, Z)]$ and its variance $\mathrm{Var}[f(\rho, Z)]$, controlled by the weighting parameter $\eta \in [0, 1]$, and subjected to a volume constraint V^*. The potentially large difference in the magnitudes of the mean and variance is accounted for by applying a logarithmic scaling to both preventing one term from disproportionately dominating the objective function by effectively scaling down both terms, while the parameter η balances the trade-off between optimizing for performance (mean) and robustness (variance), where:

- $\eta = 1$: The objective function exclusively focuses on minimizing the mean of the compliance.
- $\eta = 0$: The objective function solely targets the minimization of the standard deviation (or variance) of the compliance focusing on the robustness of the design by reducing its sensitivity to uncertainties.
- $0 < \eta < 1$: The optimization function seeks designs that are optimal on average and exhibit

controlled behavior to uncertainties.

2.3 Uncertainty quantification method using multi-fidelity

Monte Carlo estimator

The MC method estimates the mean, $\hat{s}$, and variance, $\hat{v}$, of a quantity of interest (QoI), f, given m samples as follows

$$\hat{s}_m = \frac{1}{m}\sum_{r=1}^{m} f_r, \tag{2.15}$$

$$\hat{v}_m = \frac{1}{m-1}\sum_{r=1}^{m} (f_r - \hat{s}_m)^2, \tag{2.16}$$

where $\hat{s}_m$ is the MC mean estimator or the estimated mean obtained from m samples, and f_r represents an individual sample of the QoI for a specific random input. The variance, $\hat{v}_m$, is also estimated using the same m samples. An alternative approach to estimating the variance involves using an auxiliary variable, which allows for the computation of additional statistical metrics such as correlation coefficients. This auxiliary variable, denoted as b_r, is chosen such that its mean matches the variance estimate, i.e., $\mathbb{E}[b_m] = \hat{v}_m$, and is computed using

$$b_r = \frac{m}{m-1}(f_r - \hat{s}_m)^2 \tag{2.17}$$

This method is relatively simple and easy to implement. However, the mean-squared error (MSE) of the MC method is inversely proportional to the number of samples, making it computationally infeasible for expensive-to-evaluate models like high-fidelity battery simulations. To address this limitation, the multifidelity Monte Carlo (MFMC) method [43] emerges by leveraging the speed of lower-fidelity models while maintaining or improving accuracy compared to standard MC methods. The core concept of MFMC is to combine multiple levels of model fidelity to achieve a target MSE while accelerating the computation of statistical moments for QoIs. The number of samples drawn from each model depends on its computational cost and correlation in terms of

QoIs with the highest-fidelity model. This approach accommodates various distributions and models including data such as results from experiments or sensor measurements [43].

Multifidelity Monte Carlo problem formulation

The aim of the MFMC method is to provide an unbiased estimator that can optimally exploit lower fidelity models to estimate the mean and variance of the QoIs of the highest fidelity with a given computational budget and that provides a lower MSE than MC estimator, [43].

Consider k models $\mathbb{F}_1, \ldots, \mathbb{F}_k$ with $\mathbb{F}_1$ being the high-fidelity model and $\mathbb{F}_2$ to $\mathbb{F}_k$ as the $k-1$ lower-fidelity models ordered in descending order of Pearson correlation with respect to the high-fidelity model and each model outputs N quantities of interest (QOI). We only use a lower fidelity model j in the MFMC setup if the cost $w_j \in \mathbb{R}$ of evaluating the model is lower than the cost w_{j-1} of evaluating the model $j-1$. If the models satisfy the above two conditions, then the vector of sample sizes, $\boldsymbol{m} = \{m_1, \ldots, m_k\}$, for the different models are ordered such that $0 < m_1 \leq \ldots \leq m_k$. Now let $\boldsymbol{z}_1, \ldots, \boldsymbol{z}_{m_k}$ be m_k realizations of the random variable $\boldsymbol{Z}$. Then the MFMC mean $\hat{s}_{MF}^{(l)}$ and the MFMC variance $\hat{v}_{MF}^{(l)}$ estimators for each mechanical property, l, are

$$\hat{s}_{MF}^{(l)} = \hat{s}_{1,m_1}^{(l)} + \sum_{j=2}^{k} \alpha_j^{(l)} \left(\hat{s}_{j,m_j}^{(l)} - \hat{s}_{j,m_{j-1}}^{(l)} \right), \tag{2.18}$$

$$\hat{v}_{MF}^{(l)} = \hat{v}_{1,m_1}^{(l)} + \sum_{j=2}^{k} \beta_j^{(l)} \left(\hat{v}_{j,m_j}^{(l)} - \hat{v}_{j,m_{j-1}}^{(l)} \right). \tag{2.19}$$

The superscripts indicate QoI, the subscript indicates first the model fidelity and second the number of evaluations used to compute that quantity, m_j. The control variate coefficients for the mean, $\hat{s}$, and variance, $\hat{v}$, for all QOI and for each fidelity are $\alpha_j^{(l)}$ and $\beta_j^{(l)}$, respectively. These coefficients are a function of the correlation coefficient and the variance. These control variates determine the influence of lower fidelity models on the MFMC estimator. Now, our objective is to quantify uncertainty by bounding the Mean Squared Error (MSE) across all quantities of interest $MSE^{(l)}$ in a single MFMC run. The MSE is the sum of individual MSEs for each QoI, scaled by a variable $\delta^{(l)}$ to assign equal importance to all QoIs.

$$\mathscr{J} = \sum_{l=1}^{N} \delta^{(l)} MSE^{(l)} \tag{2.20}$$

The total MSE for each quantity of interest is defined as

$$\mathrm{MSE}^{(l)} = \mathrm{MSE}\left(f^{(l)}\right) + \xi^{(l)}\,\mathrm{MSE}\left(b^{(l)}\right), \tag{2.21}$$

and $\xi^{(l)}$ is the scaling factor between mean and variance MSEs for each QOI and has a similar function to $\delta^{(l)}$. If the MFMC estimator is unbiased and the variance is finite, it is possible to rewrite the MSE as,

$$\mathrm{MSE}^{(l)} = \mathbb{V}ar\left(\hat{s}_{MF}^{(l)}\right) + \xi^{(l)}\mathbb{V}ar\left(\hat{v}_{MF}^{(l)}\right), \tag{2.22}$$

$\delta^{(l)}$ is calculated as the ratio of the maximum mean to the mean of each QoI calculated from the model with highest fidelity, and $\xi^{(l)}$ is the absolute value of the ratio of the mean to the variance of the auxiliary variable for each QoI calculated from each fidelity.

$$\delta^{(l)} = \left| \frac{\max\left(\mathbb{E}\left[f_{1,n_{init}}^{(l)}\right]\right)}{\mathbb{E}\left[f_{1,n_{init}}^{(l)}\right]} \right|, \quad \xi^{(l)} = \left| \frac{\mathbb{E}\left[f_{1,n_{init}}^{(l)}\right]}{\mathbb{E}\left[b_{1,n_{init}}^{(l)}\right]} \right|. \tag{2.23}$$

Lastly, according to *Lemma 3.3* in [43], the variance for the MFMC estimator can be written as,

$$\mathbb{V}ar\left(\hat{s}_{MF}^{(l)}\right) = \frac{\sigma_1^{(l)^2}}{m_1} + \sum_{j=1}^{k} \left(\frac{1}{m_{j-1}} - \frac{1}{m_j}\right)\left(\alpha_j^{(l)^2}\sigma_j^{(l)^2} - 2\alpha_j^{(l)}\rho_{1,j}^{(l)}\sigma_1^{(l)}\sigma_j^{(l)}\right) \tag{2.24}$$

$$\mathbb{V}ar\left(\hat{v}_{MF}^{(l)}\right) = \frac{\tau_1^{(l)^2}}{m_1} + \sum_{j=2}^{k} \left(\frac{1}{m_{j-1}} - \frac{1}{m_j}\right)\left(\beta_j^{(l)^2}\tau_j^{(l)^2} - 2\beta_j^{(l)}q_{1,j}^{(l)}\tau_1^{(l)}\tau_j^{(l)}\right) \tag{2.25}$$

As a result of equations (2.24) and (2.25), the MSE for each QoI can be rewritten as,

$$
\begin{aligned}
\mathrm{MSE}^{(l)} = \frac{\sigma_1^{(l)^2}}{m_1} + \sum_{j=1}^{k}\left(\frac{1}{m_{j-1}} - \frac{1}{m_j}\right)\left(\alpha_j^{(l)^2}\sigma_j^{(l)^2} - 2\alpha_j^{(l)}\rho_{1,j}^{(l)}\sigma_1^{(l)}\sigma_j^{(l)}\right) \\
+ \xi^{(l)}\left(\frac{\tau_1^{(l)^2}}{m_1} + \sum_{j=2}^{k}\left(\frac{1}{m_{j-1}} - \frac{1}{m_j}\right)\left(\beta_j^{(l)^2}\tau_j^{(l)^2} - 2\beta_j^{(l)}q_{1,j}^{(l)}\tau_1^{(l)}\tau_j^{(l)}\right)\right)
\end{aligned}
\tag{2.26}
$$

We then formulate the minimization problem of the MSE to find the optimal control variate coefficients and sampling size, leading to a closed-form solution involving the CPU time, w_j, the Pearson correlation coefficients, $\rho_{1,j}^{(l)}$ and $q_{1,j}^{(l)}$ (for $\hat{s}_{MF}^{(l)}$ and $\hat{v}_{MF}^{(l)}$, respectively), and the variances $\sigma_j^{(l)^2}$ and $\tau_j^{(l)^2}$. For a full derivation, see [14].

$$
\min \ \mathscr{J}(\boldsymbol{m}, \alpha_1^{(1)}, \ldots, \alpha_k^{(1)}, \ldots, \alpha_k^{(N)}, \beta_1^{(1)}, \ldots, \beta_k^{(1)}, \ldots, \beta_k^{(N)}) \tag{2.27}
$$

$$
\begin{aligned}
\textbf{s.t:} \qquad m_{j-1} - m_j &\leq 0 \\
-m_1 &\leq 0 \\
\boldsymbol{w^T m} &= p.
\end{aligned}
$$

Optimization problem solution

The first step towards solving this optimization problem is to formulate the augmented Lagrangian objective function, which is a function of the same variables as our original objective function plus the Lagrange multipliers.

$$
\mathscr{L}\left(m, \alpha^{(l)}, \beta^{(l)}\right) = \sum_{l=1}^{QoI} \delta^{(l)} \mathrm{MSE}^{(l)} + \lambda\left(\omega^\top m - p\right) - \mu_1 m_1 + \sum_{j=1}^{k} \mu_j\left(m_{j-1} - m_j\right) \tag{2.28}
$$

The optimal control variate coefficients come from the partial derivatives of the Lagrangian function with respect to the control variate coefficients.

$$\frac{\partial \mathscr{L}}{\partial \alpha_j^{(l)}} = 2\alpha_j^{(l)} \sigma_j^{(l)^2} - 2\rho_{1,j}^{(l)} \sigma_1^{(l)} \sigma_j^{(l)} = 0 \tag{2.29}$$

$$\frac{\partial \mathscr{L}}{\partial \beta_j^{(l)}} = 2\beta_j^{(l)} \tau_j^{(l)^2} - 2q_{1,j}^{(l)} \tau_1^{(l)} \tau_j^{(l)} = 0 \tag{2.30}$$

This leads to the solution for the optimal control variate coefficient, denoted by $*$ and is expressed as,

$$\alpha_j^{(l)^*} = \rho_{1,j}^{(l)} \frac{\sigma_1^{(l)}}{\sigma_j^{(l)}}, \tag{2.31}$$

$$\beta_j^{(i)^*} = q_{1,j}^{(i)} \frac{\tau_1^{(i)}}{\tau_j^{(i)}}, \tag{2.32}$$

The optimal control variate coefficients expressions make it possible to simplify the equation for the MSE, (2.26), which enables rewriting it as,

$$\mathrm{MSE}^{(l)} = \frac{\sigma_1^{(l)^2} + \xi^{(l)} \tau_1^{(l)^2}}{m_1} - \sum_{j=1}^{k} \left(\frac{1}{m_{j-1}} - \frac{1}{m_j} \right) \left(\rho_{1,j}^{(l)^2} \sigma_1^{(l)^2} + \xi^{(l)} q_{1,j}^{(l)^2} \tau_1^{(l)^2} \right). \tag{2.33}$$

From KKT conditions primal feasibility, dual feasibility, and complementary slackness properties, i.e., $m_{j-1} - m_j \leq 0$, $\mu_j \geq 0$ and $\mu_j \left(m_{j-1} - m_j \right) = 0$, we obtain $\mu_j = 0, \quad \forall j \geq 2$. Similarly, for μ_1, from the relationship between the sampling size and computational cost $\boldsymbol{w^T m} = p$, we get that m_1 must be positive, thus $\mu_1 = 0$. Therefore, the augmented Lagrangian equation reduces to,

$$\mathscr{L}\left(m, \alpha^{(l)}, \beta^{(l)}\right) = \sum_{l=1}^{QoI} \delta^{(l)}\, \mathrm{MSE}^{(l)} + \lambda \left(\boldsymbol{\omega}^\top \boldsymbol{m} - p \right) \tag{2.34}$$

The value of λ comes from the derivative of the Lagrangian augmented function with respect to m_1

$$\frac{\partial \mathscr{L}}{\partial m_1} = \frac{\partial}{\partial m_1} \sum_{l=1}^{N} \delta_l \, \text{MSE}^{(l)} + \lambda \omega_1 = 0 \tag{2.35}$$

From equation (2.35) we obtain λ as a function of the MSE for each QoI and the scaling factor, $\delta^{(l)}$. We can replace the value of the MSE for each QoI by the expression in equation (2.33). To obtain the value of the Lagrange multiplier as a function of the sampling size, the variance of the QoI and the auxiliary variables and the correlation between fidelity models.

$$\begin{aligned}
\lambda &= -\frac{1}{\omega_1} \sum_{l=1}^{N} \delta^{(l)} \frac{\partial \, \text{MSE}^{(l)}}{\partial m_1} \\
\lambda &= \frac{1}{\omega_1} \sum_{l=1}^{N} \delta^{(l)} \left(\frac{\sigma_1^{(l)^2} + \xi^{(l)} \tau_1^{(l)^2}}{m_1^2} - \frac{1}{m_1^2} \left(\rho_{1,2}^{(l)^2} \sigma_1^{(l)^2} + \xi^{(l)} q_{1,2}^{(l)^2} \tau_1^{(l)^2} \right) \right)
\end{aligned} \tag{2.36}$$

From the equation above it is possible to factor out m_1, which we will later use to obtain the sampling ratios.

$$\lambda = \frac{1}{\omega_1 m_1^2} \sum_{l=1}^{N} \delta^{(l} \left[\sigma_1^{(l)^2} \left(1 - \rho_{1,2}^{(l)^2} \right) + \xi^{(2)} \tau_1^{(l)^2} \left(1 - q_{1,2}^{(l)^2} \right) \right] \tag{2.37}$$

Up to this point in the optimization we have obtained the optimal values of the control variate coefficients and we have calculated the optimal value for the Lagrange multipliers. The only remaining unknown is the optimal sampling sizes for each fidelity model. To obtain these variables we take the derivative of the Lagrangian function with respect to the sampling size variables, $m_j \forall j \geq 2$.

$$\frac{\partial \mathscr{L}}{\partial m_j} = \frac{\partial}{\partial m_j} \sum_{l=1}^{Q} \delta^{(l)} \, \text{MSE}^{(l)} + \lambda \omega_j = 0. \tag{2.38}$$

Expanding the equation above using equation (2.33) and taking the derivative with respect m_j we get,

$$\sum_{l=1}^{N} \frac{\delta^{(l)}}{m_j^2} \left[-\rho_{1,j}^{(l)^2} \sigma_1^{(l)^2} - \xi^{(l)} q_{1,j}^{(l)} \tau_1^{(l)^2} + \rho_{1,j+1}^{(l)^2} \sigma_j^{(l)^2} + \xi^{(l)} q_{1,j+1}^{(l)} \tau_j^{(l)^2}\right] + \lambda \omega_j = 0. \tag{2.39}$$

The last step to get the expression for the optimal sampling ratios is to substitute the value of λ from equation (2.37).

$$\sum_{l=1}^{N} \frac{\delta^{(l)}}{m_j^2} \left[-\rho_{1,j}^{(l)^2} \sigma_1^{(l)^2} - \xi^{(l)} q_{1,j}^{(l)} \tau_1^{(l)^2} + \rho_{1,j+1}^{(l)^2} \sigma_j^{(l)^2} + \xi^{(l)} q_{1,j+1}^{(l)} \tau_j^{(l)^2}\right] + \\ \frac{\omega_j}{\omega_1 m_1^2} \sum_{l=1}^{N} \delta^{(l} \left[\sigma_1^{(l)^2} \left(1 - \rho_{1,2}^{(l)^2}\right) + \xi^{(2)} \tau_1^{(l)^2} \left(1 - q_{1,2}^{(l)^2}\right)\right]. \tag{2.40}$$

Finally, by expressing the quotient of sampling size for fidelity j over the sampling size for the highest fidelity, we obtain the optimal sampling ratios r_j, which depend only on statistical and known quantities.

$$r_j^{2*} = \frac{m_j^{2*}}{m_1^{2*}} = \frac{\omega_1}{\omega_j} \frac{\sum_{l=1}^{N} \delta^{(l)} \left[\sigma_1^{(l)^2} \left(\rho_{1,j}^{(l)^2} - \rho_{1,j+1}^{(l)^2}\right) + \xi^{(l)} \tau_1^{(l)^2} \left(q_{1,j}^{(l)^2} - q_{1,j+1}^{(l)^2}\right)\right]}{\sum_{l=1}^{N} \delta^{(l)} \left[\xi^{(l)} \left(1 - \rho_{1,2}^{(l)^2}\right) + \xi^{(l)} \tau_j^{(l)^2} \left(1 - q_{1,2}^{(l)^2}\right)\right]} \tag{2.41}$$

Once the optimal sampling ratio is obtained, the only unknown variable is m_1 which is obtained through the equation for the budget and the optimal sampling ratio concept.

$$\boldsymbol{\omega}^\top \boldsymbol{m} = p \Rightarrow \boldsymbol{\omega}^\top \boldsymbol{r} m_1 - p = 0 \tag{2.42}$$

Thus, the optimal sampling size for the highest fidelity model is a function of the computational budget, the computational cost and the optimal sampling ratio.

$$m_1^* = \frac{p}{\boldsymbol{\omega}^\top \boldsymbol{r}^*} \tag{2.43}$$

$$m_j = m_1 r_j \tag{2.44}$$

Once we have obtained all the arguments that minimize the MSE we can recompute it by just plugging back the optimal arguments' values into equation (2.20).

$$A^{(l)} = \sigma_1^{(l)^2} + \xi^{(l)} \tau_1^{(l)^2} + \sum_{j=2}^{k} \left(\frac{1}{r_j^*} - \frac{1}{r_{j-1}^*} \right) \left(\rho_{1,j}^{(l)^2} \sigma_1^{(l)^2} + \xi^{(l)} q_{1,i}^{(l)^2} \tau_1^{(l)^2} \right) \tag{2.45}$$

$$p_{\text{req}} = \frac{\boldsymbol{w}^T \boldsymbol{r}^*}{\mathscr{J}} \sum_{l=1}^{N} \delta^{(l)^T} A^{(l)}. \tag{2.46}$$

The variable $A^{(l)}$ contains the dependencies with respect to the correlation coefficients and variances. It is included for clarity purposes.

Finally, the scaling factor $\delta^{(l)}$ is a heuristic problem-dependent parameter. This formulation recovers automatically the one QoI case by setting δ to the scalar value of one.

This procedure shows the derivation of optimal MFMC arguments to minimize the MSE given a computational budget. However, it is also possible to solve for computational budget minimization subject to a given MSE. In both cases, the solutions are the same and the only change occurs in equation (2.46) where we swap places between p_{req} and $\mathscr{J}$.

Model selection

The model selection is an algorithm that enables choosing the set of fidelity models that provide the minimum computational budget given an MSE constraint or vice-versa. This algorithm follows the one in [43] and it is adapted to this method extension.

The MFMC method works based on the assumption that the models are ordered in descending absolute correlation. Chaudhuri [14] modified this criterion to include the correlation of the auxiliary variable as $|\rho_{1,1}|+|q_{1,1}|>\cdots>|\rho_{1,k}|+|q_{1,k}|$. For this problem, we follow this criterion using the correlation of the largest QoI as for the micromechanics problem gave the smallest computational budget.

Once the models are ordered by correlation we delete any model with a lower correlation that has higher computational cost to reduce the number of model combination to evaluate as the combinatorial problem scales with, 2^k. Then we proceed to evaluate the computational budget, according to equation (2.46), of all remaining fidelities combinations and checking for each of them that they meet the condition of minimizing the computational budget or MSE, depending on how we formulated the problem. This condition is based on the problem constrain $m_{j-1}-m_j \leq 0$ and $m_1 \geq 0$ which using equation (2.41) becomes,

$$\frac{w_{j-1}}{w_j} > \frac{\sum_{l=1}^{N} \delta^{(l)} \left[\sigma_1^{(l)^2}\left(\rho_{1,j-1}^{(l)^2}-\rho_{1,j}^{(l)^2}\right)+\xi^{(l)}\tau_1^{(l)^2}\left(q_{1,j-1}^{(l)^2}-q_{1,j}^{(l)^2}\right)\right]}{\sum_{l=1}^{N} \delta^{(l)} \left[\sigma_1^{(l)^2}\left(\rho_{1,j}^{(l)^2}-\rho_{1,j+1}^{(l)^2}\right)+\xi^{(l)}\tau_1^{(l)^2}\left(q_{1,j}^{(l)^2}-q_{1,j+1}^{(l)^2}\right)\right]} \tag{2.47}$$

Here we present an algorithm that summarizes all the steps and checks in order to implement MFMC.

Algorithm 1. MFMC algorithm

```
Build $\mathbb{F}_1, \ldots, \mathbb{F}_k$.
Define the RVs, $\boldsymbol{Z}$, and sample $n_{init}$ times using a truncated normal distribution (number of samples heuristically chosen and problem dependent)
Run models, $\mathbb{F}_1, \ldots, \mathbb{F}_k$, for each $n_{init}$ samples (total runs = number of samples $\times$ number of models) to obtain the quantities of interest, QoI, $f_{j,r}^{(i)}$ and its sensitivity $\frac{df_{j,r}^{(i)}}{d\mathbf{d}_j}$.
Compute the auxiliary variable $b_{j,r}^{(l)}$ with equation (2.17)
Compute $\sigma_j^{(l)}$, and $\rho_{1,j}^{(l)}$, $\tau_j^{(l)}$, and $q_{1,j}^{(l)}$, based on $f_{j,r}^{(l)}$ and $b_{j,r}^{(l)}$, from those $n_{init}$ initial samples.

Order the models in descending order of correlation coefficient for the first QoI as, $|\rho_{1,1}| + |q_{1,1}| > \cdots > |\rho_{1,j}| + |q_{1,j}|$ and delete the models with a higher computational budget than a higher fidelity one.
Evaluate equations (2.41), and (2.46) for all remaining models' combination and choose the one with smallest budget, $p_{\text{req}}$ if it satisfies equation (2.47).
Compute $\alpha_j^{(l)}$ and $\beta_j^{(l)}$ using equations (2.31), (2.32)
Compute the optimal sampling size using equations (2.43), (2.44)
Run all fidelities according to $\mathbf{m}^*$ from previous step.
Calculate the QoIs mean and variance using equations (2.18) and (2.19), respectively
```

Chapter 2, in part is currently being prepared for submission for publication of the material. Diaz-Flores Caminero, Alvaro; Ismail, Hussein; Chadhuri, Anirban; Kim, H. Alicia. The thesis author was the primary investigator and author of this material.

Chapter 3

Numerical implementation

3.1 Multi-fidelity Monte Carlo for micromechanics

In this study, we utilize the Multi-Fidelity Monte Carlo (MFMC) method to quantify uncertainties in the homogenized elastic tensor $\boldsymbol{C}^*$ derived from micromechanical models. The entries of the elastic tensor, referred to as QoIs, including the diagonal terms C_{11}, C_{22}, C_{66} representing the direct stiffness in the xx-, yy-, and shear directions, and the off-diagonal term C_{12}, C_{16}, C_{26} describing the coupling effects between stresses and strains in orthogonal directions, and between normal stresses and shear strains, respectively.

We consider two primary random variables (RVs) representing the material properties of the constituents: the longitudinal Young's modulus of the fiber $E_{11}^{(f)}$, and the Young's modulus of the isotropic matrix $E^{(m)}$. Each RV is modeled using a truncated normal distribution characterized by a mean μ, a standard deviation $\sigma = \gamma\mu$ where γ denotes the coefficient of variation, noting that we are not limited to this RV selection and probability distribution type.

Two micromechanical models of differing fidelities are used: a high-fidelity model ($\mathbb{F}_1$) utilizing the High-Fidelity Generalized Method of Cells (HFGMC) with a detailed discretization of the Representative Unit Cell (RUC), and a low-fidelity model ($\mathbb{F}_2$) employing the Generalized Method of Cells (GMC) with a coarser discretization.

The effective constitutive tensor $\boldsymbol{C}^*$ obtained from the micromechanical models is initially aligned with the fiber's local coordinate system. To integrate this tensor into the global coordinate system, we perform a rotation using a transformation matrix $\boldsymbol{T}_{\boldsymbol{\theta}}$ that accounts for the fiber orientation angle θ. Following the rotation, the mean and variance of the QoIs are calculated from the rotated constitutive tensor for a RUC with the fiber oriented at angle θ.

$$\mathbb{E}[\boldsymbol{C}^*_{\theta}] = \mathbb{E}[\boldsymbol{T}_{\boldsymbol{\theta}} \boldsymbol{C}^*_{x'y'z'} \boldsymbol{T}^T_{\boldsymbol{\theta}}], \tag{3.1}$$

$$\mathbb{V}\text{ar}[\boldsymbol{C}^*_{\theta}] = \mathbb{V}\text{ar}[\boldsymbol{T}_{\boldsymbol{\theta}} \boldsymbol{C}^*_{x'y'z'} \boldsymbol{T}^T_{\boldsymbol{\theta}}]. \tag{3.2}$$

This framework allows computations to be executed on-demand for specific angles or by utilizing a discretized set of θ values that are precomputed and stored as database of mean and variance of each QoIs for the set of orientation angles for a subsequent analyses.

Algorithm 2. MFMC for Micromechanics

```
Build micromechanical fidelity models $\mathbb{F}_1$, $\mathbb{F}_2$ with different discretizations.
Define random variables for material properties (e.g., $E_{11}^{(f)}$, $E^{(m)}$) and sample them using a truncated normal distribution.
Run models $\mathbb{F}_1$, $\mathbb{F}_2$, etc., for each sample to obtain the homogenized elastic tensor $\boldsymbol{C}^*$, according to Algortihm 1.
Compute mean $\mathbb{E}[\boldsymbol{C}^*_{\theta}]$ and variance Var$[\boldsymbol{C}^*_{\theta}]$ using MFMC estimators (Eqs.(2.18), (2.19)).
Store the computed statistical moments for each orientation $\theta$.
```

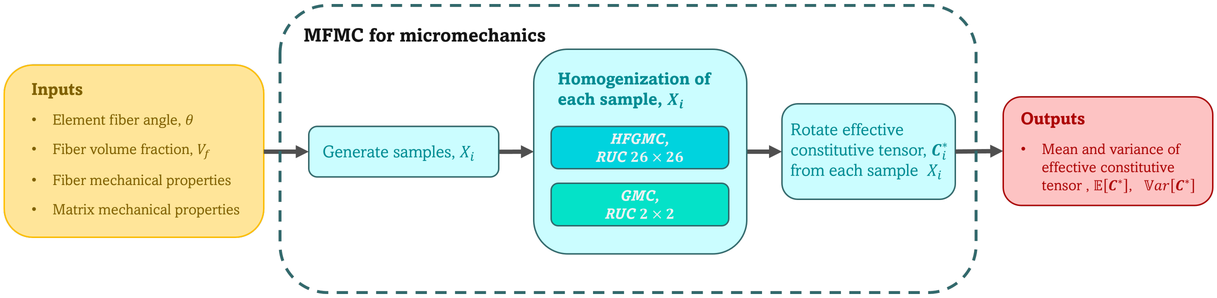

Figure 3.1. mfRTO workflow.

3.1.1 Compliance MFMC

In this section, we utilize the Multi-Fidelity Monte Carlo (MFMC) method to quantify uncertainties for the structural compliance f, our primary Quantity of Interest, arising from uncertainties in material properties.

Consider multiple finite element models with different levels of fidelity, such that the high-fidelity model ($\mathbb{F}_1$) uses a finely discretized finite element mesh to provide accurate results at a higher computational cost, and lower-fidelity models ($\mathbb{F}_2, \mathbb{F}_3, \ldots$) use coarser meshes that are computationally cheaper but less accurate.

Different fidelity levels are created based on the high-fidelity model by implementing a blurring (mapping) procedure for the volume fraction ρ and the fiber orientation θ, similar to the mapping approach described in [30]. The lower-fidelity design variables are computed by mapping from the high-fidelity design using a convolutional smoothing approach:

$$\boldsymbol{\rho}^{(i)} = \boldsymbol{H}^{(i)}_{(1)} \boldsymbol{\rho}^{(1)}, \quad \boldsymbol{\theta}^{(i)} = \boldsymbol{H}^{(i)}_{(1)} \boldsymbol{\theta}^{(1)}. \tag{3.3}$$

where $\boldsymbol{H}^{(i)}_{(1)}$ is a mapping matrix defined as:

$$H_{mn} = \frac{w_{mn}}{\sum_{n=1}^{N^{(1)}} w_{mn}}, \quad w_{mn} = \begin{cases} 1, & \text{if } \|\boldsymbol{x}_m^{(i)} - \boldsymbol{x}_n^{(1)}\| \leq r, \\ 0, & \text{otherwise}, \end{cases} \tag{3.4}$$

where $\boldsymbol{x}_n^{(1)}$ and $\boldsymbol{x}_m^{(i)}$ represent the centroids of elements in the high-fidelity and i-th fidelity models, respectively, and r is the influence radius. Figure 3.2 illustrates the mapping algorithm, showing the interaction between two overlapping meshes: the high-fidelity mesh (dashed red) and the low-fidelity mesh (solid blue). The centroids of the high-fidelity elements are labeled as $A1$ to $A16$ (with $A17$ to $A64$ omitted for clarity), while the centroids of the low-fidelity elements are labeled as $B1$ to $B4$. The neighborhood of influence for the centroid $B1$ is represented by the yellow circle, covering all high-fidelity centroids within the specified radius r.

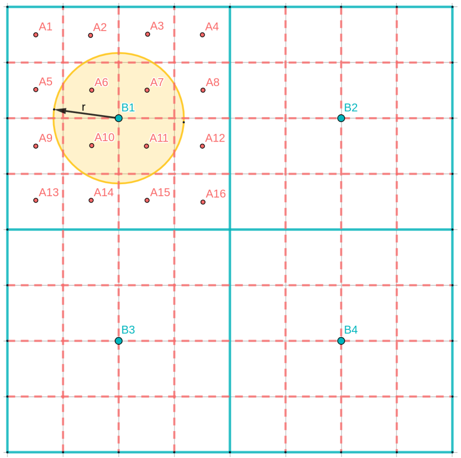

Figure 3.2. Convolutional smoothing mapping representation.

In Fig.(3.2), there are two overlapping meshes: the high-fidelity dashed red mesh whose elements centroids are A1-A16 (A17-A64 are not represented), and the low-fidelity solid blue mesh whose elements centroids are B1-B4. Finally, the golden circle shows the neighborhood of influence around centroid B1.

The components of the effective constitutive tensor $\boldsymbol{C}^*_{(\theta)}$ are used as random variables representing, to model material uncertainties, with each unique fiber orientation θ treated as a distinct material. Fiber orientations across different fidelities are collected into a set $\{\theta_1, \theta_2, \dots, \theta_t\}$, where t denotes the total number of unique orientations, determining the number of material tensors constributing to the total random variables in the problem.

For each orientation θ, the mean $\mathbb{E}[\boldsymbol{C}^*(\theta)]$ and variance $\mathbb{V}\text{ar}[\boldsymbol{C}^*(\theta)]$ of the effective constitutive tensor are required to define the stochastic properties. If the statistical moments for a specific orientation are precomputed, they are used directly. For orientations without precomputed data, MFMC simulations at the micromechanical level are used to determine the required statistical moments as described in section 3.1. These moments are then used to define the effective material properties for the corresponding orientation.

Let $\boldsymbol{Z_\theta}$ be the vector containing input random variables for a specific fiber orientation in element e, such that $\boldsymbol{Z}_\theta = \left[C_{\theta,11}, C_{\theta,22}, C_{\theta,12}, C_{\theta,13}, C_{\theta,23}, C_{\theta,33}\right]$ represent the six random variables of the effective constitutive tensor sampled from a corresponding distribution. Each input random variable has a set of m_j samples used to evaluate fidelity model j. We evaluate our model for each set of samples for each angle we have:

$$\boldsymbol{z}_r = \left[C_{\theta,11}, C_{\theta,22}, C_{\theta,12}, C_{\theta,13}, C_{\theta,23}, C_{\theta,33}\right]_r \quad \text{for } r = 1, 2, \ldots, m_j.$$

The global stiffness matrix $\boldsymbol{K}_{j,r}$ for each fidelity model is constructed by assembling the element stiffness matrices $(\boldsymbol{K}_e)_{j,r}$, where:

$$(\boldsymbol{K}_e)_{j,r} = \int_{\Omega_e} \boldsymbol{B}^T (\boldsymbol{C}_{\boldsymbol{\theta}})_r \boldsymbol{B} \, d\Omega_e, \tag{3.5}$$

Here, $\boldsymbol{B}$ is the strain-displacement matrix, and $(\boldsymbol{C}_{\boldsymbol{\theta}})_r$ is the constitutive tensor corresponding to θ for sample r. The structural compliance for each fidelity model and sample is computed as:

$$f_{j,r} = {\boldsymbol{U}_{j,r}}^T \boldsymbol{F}_{j,r}, \tag{3.6}$$

where $\boldsymbol{U}_{j,r}$ is the displacement vector obtained by solving:

$$\boldsymbol{K}_{j,r} \boldsymbol{U}_{j,r} = \boldsymbol{F}_{j,r}. \tag{3.7}$$

Using control variate coefficients in equations (2.31) and (2.32), the compliance results from all fidelity models are combined to estimate the mean $\mathbb{E}[f]$ in equation (2.18) and variance $\mathbb{V}\text{ar}[f]$ in equation (2.19).

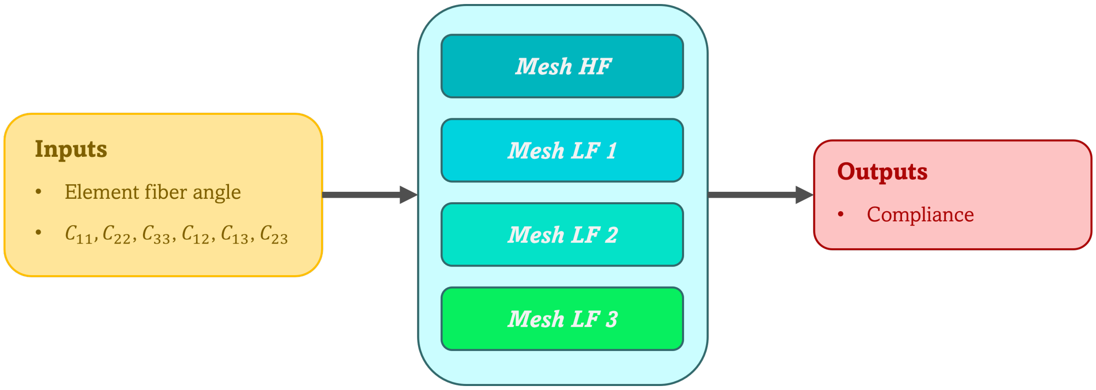

Figure 3.3. Models with varying fidelity for FEA analysis.

By utilizing the MFMC method within the topology optimization framework, the mean and variance of material properties at the microscale and macroscale are quantified, enabling the propagation of material uncertainties from the microscale to the uncertainty quantification of structural compliance at the macroscale. In the same time, fiber orientations are iteratively aligned with principal stress directions to minimize the strain energy. The workflow of the RTO algorithm, shown in Figure 3.4, connects these components, with more detailed algorithmic steps outlined in Algorithm 3.

Algorithm 3. Robust Multi-Scale Topology Optimization Algorithm

```
1: Define a set of fiber orientations $\{\theta_1, \theta_2, \dots, \theta_t\}$.
2: Apply MFMC to compute the mean $\mathbb{E}[\boldsymbol{C}^*(\theta)]$ and variance $\mathrm{Var}[\boldsymbol{C}^*(\theta)]$ of the homogenized elastic tensor for each orientation $\theta$ (Algorithm 2).
3: Build high-fidelity model $\mathbb{F}_1$ and lower-fidelity models $\mathbb{F}_2$, ..., $\mathbb{F}_k$ by changing the mesh discretization.
4: Initialize or update fiber orientations by aligning fibers with principal stress directions using the iterative procedure for the high-fidelity model $\mathbb{F}_1$ (Section 2.1.3).
5: Map design variables and fiber orientations from $\mathbb{F}_1$ to lower fidelities using convolutional smoothing (Eq. (3.3)).
6: Define the set of unique orientations and random variables $\boldsymbol{Z}$ representing uncertainties in material properties and sample them (use the stored data from 2, or run MFMC for needed $\theta$).
7: Assign material properties to each element based on computed $\mathbb{E}[\boldsymbol{C}^*(\theta)]$ and $\mathbb{V}ar[\boldsymbol{C}^*(\theta)]$.
8: Use MFMC to compute mean $\hat{s}_{MF}$ and variance $\hat{v}_{MF}$ of compliance (Section 3.1.1).
9: Compute sensitivities $\frac{dJ}{d\boldsymbol{\phi}^{(1)}}$ required for optimization (Section 3.1.2).
10: Update design variables $\boldsymbol{\phi}^{(1)}$ using an optimization algorithm (e.g., gradient-based method).

11: Return to step 4 until convergence criteria are met.
```

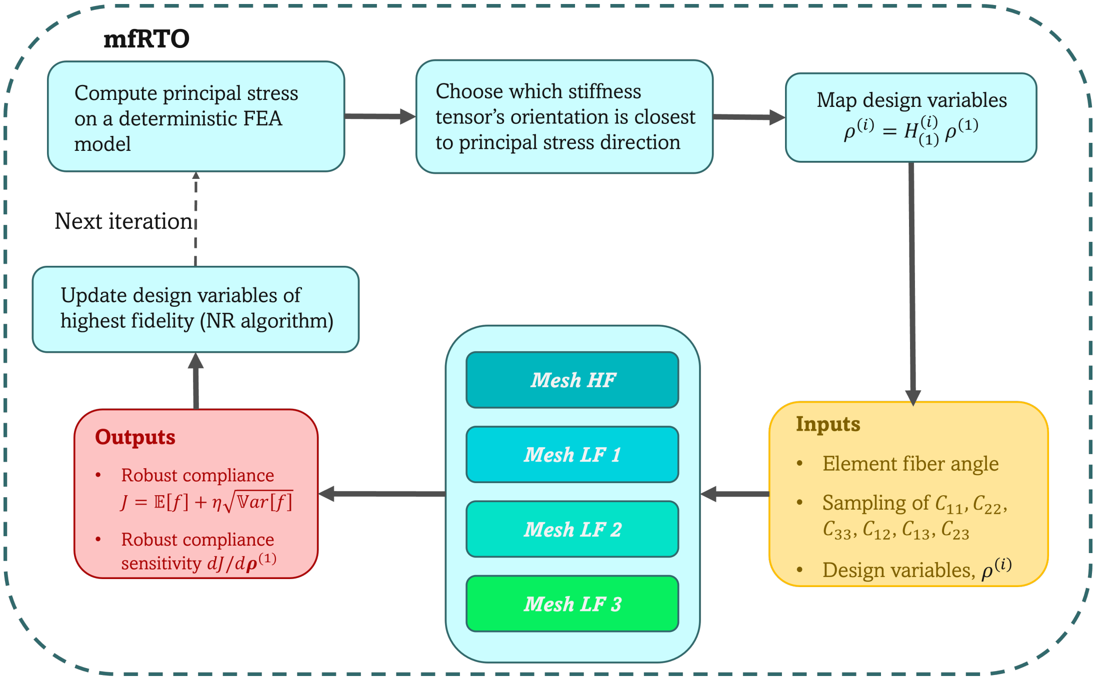

Figure 3.4. mfRTO workflow.

In summary, the forward analysis involves creating multiple models with varying fidelity levels based on mesh resolution. Each fidelity model is evaluated according to section 3.1.1, and these evaluations are combined using the control variate coefficients, equations (2.31) and (2.32), to estimate the mean and variance as given by equations (2.18) and (2.19). The next step involves determining the procedure for updating the design in each iteration.

3.1.2 sensitivities

The shape sensitivities of the objective function $\frac{\partial J}{\partial \Omega}$ and the constraints $\frac{\partial g}{\partial \Omega}$ are needed for solving the sub-optimization problem to obtain $V_{n,p}$ at each iteration of the topology optimization. These sensitivities are expressed using the chain rule, for example:

$$\frac{dJ}{d\Omega_p} = \sum_{e=1}^{N_e} \frac{dJ}{d\rho_e}\frac{d\rho_e}{d\Omega_p}, \qquad \frac{d\rho_e}{d\Omega_p} \approx \frac{\rho_e - \rho_e^0}{\delta_p}, \tag{3.8}$$

where N_e is the number of elements, $\frac{dJ}{d\rho_e}$ is the sensitivity with respect to the volume fraction ρ_e, and $\frac{d\rho_e}{d\Omega_p}$ is determined using a perturbation scheme. In this scheme, δ_p denotes a perturbation in the normal direction at boundary point p, and ρ_e^0 is the volume fraction of the element after perturbing the level-set function.

The sensitivity of the objective function (2.14a) with respect to the volume fraction is,

$$\frac{dJ}{d\rho_1} = \frac{(\eta) d\hat{s}_{MF}}{d\rho_1} + \frac{(1-\eta)}{2\hat{v}_{MF}} \frac{d\hat{v}_{MF}}{d\mathbf{d}_1}. \tag{3.9}$$

where the sensitivity of the MFMC mean and variance estimator is obtained through the derivative of equations (2.18) and (2.19), such that $H_{1,j} = \frac{d\mathbf{d}_j}{d\mathbf{d}_1}$ is the mapping function from the highest fidelity design variables to a lower fidelity j ones.

$$\frac{d\hat{s}_{MF}}{d\rho_1} = \frac{d\hat{s}_{1,m_1}}{d\rho_1} + \sum_{j=2}^{k} \alpha_j \left(\frac{d\hat{s}_{j,m_j}}{d\rho_j} - \frac{d\hat{s}_{j,m_{j-1}}}{d\rho_j} \right) H_{1,j}, \tag{3.10}$$

$$\frac{d\hat{v}_{MF}}{d\rho_1} = \frac{d\hat{v}_{1,m_1}}{d\rho_1} + \sum_{j=2}^{k} \beta_j \left(\frac{d\hat{v}_{j,m_j}}{d\rho_j} - \frac{d\hat{v}_{j,m_{j-1}}}{d\rho_j} \right) H_{1,j}, \tag{3.11}$$

For each fidelity, the sensitivity of the mean and variance of any fidelity with respect to that fidelity's design variable, computed with m_j samples is:

$$\frac{d\hat{s}_{j,m_j}}{d\rho_\mathbf{j}} = \frac{d}{d\rho_\mathbf{j}} \left(\frac{1}{m_j} \sum_{r=1}^{m_j} f_{r_j} \right) = \frac{1}{m_j} \sum_{r=1}^{m_j} \frac{df_{r_j}}{d\rho_\mathbf{j}} = \mathbb{E}\left[\frac{df_{r_j}}{d\rho_\mathbf{j}} \right] \tag{3.12}$$

and the variance sensitivity for any fidelity model is

$$\frac{d\hat{v}_{m_j}}{d\rho_\mathbf{j}} = \frac{d}{d\rho_\mathbf{j}} \mathbb{E}[b_{r_j}] = \mathbb{E}\left[\frac{d\,b_{r_j}}{d\rho_\mathbf{j}} \right] \tag{3.13}$$

where the sensitivity of the auxiliary variable is

$$\frac{d\,b_{r_j}}{d\rho_{\mathbf{j}}} = \frac{d}{d\rho_{\mathbf{j}}}\left[\frac{m_j}{m_j-1}(f_{r_j}-\hat{s}_{m_j})^2\right] = \frac{2m_j}{m_j-1}(f_{r_j}-\hat{s}_{m_j})\left(\frac{d\,f_{r_j}}{d\rho_{\mathbf{j}}}-\frac{d\,\hat{s}_{m_j}}{d\rho_{\mathbf{j}}}\right) \tag{3.14}$$

Chapter 3, in part is currently being prepared for submission for publication of the material. Diaz-Flores Caminero, Alvaro; Ismail, Hussein; Chadhuri, Anirban; Kim, H. Alicia. The thesis author was the primary investigator and author of this material.

Chapter 4

Results and discussion

4.1 Composite Materials Uncertainty Quantification Using Multifidelity Monte Carlo

Mechanical properties of composite constituents exhibit inherent uncertainties. We use the Multi-fidelity Monte Carlo (MFMC) method to accelerate the estimation of statistical moments in this example and demonstrate the performance of MFMC in micromechanics uncertainty quantification across multiple mechanical properties, highlighting significant speedup over MC. We examine the influence of input variances on speedup, compare estimated mean values with nominal and MC-based results, and evaluate the variance of the MFMC estimator against the MC estimator. Additionally, for reproducibility, we present the mean and variance of mechanical properties for selected fiber orientations.

Problem Definition

The composite material under study consists of IM7 fibers embedded in 8552 epoxy resin, with a fiber volume fraction of 0.57. The fiber is modeled as a transversely isotropic material, while the resin is treated as isotropic. Nominal mechanical property values are obtained from [2] and summarized in Table 4.1.

Table 4.1. Constituent Nominal Mechanical Properties. All units are in GPa.

	Material	E_{11}	E_{22}	G_{12}	ν_{12}	ν_{23}	Volume Fraction
Fiber	IM7	262	11.8	18.9	0.17	0.21	0.57
Matrix	8552	4.67	4.67	1.61	0.45	0.45	0.43

To quantify uncertainty, variability is introduced in E_{11} for the fiber and E for the matrix. These parameters are sampled from a truncated Gaussian distribution, ensuring non-negative mechanical properties. The distribution parameters are detailed in Table 4.2, with nominal values taken from Table 4.1.

Table 4.2. Distribution Definitions: Standard Deviation (STD), Lower Bound (LB), and Upper Bound (UB) as Percentages of Mean Values.

	Case 1	Case 2
Distribution	Truncated Normal	Truncated Normal
Mean	Values from Table 4.1	Values from Table 4.1
STD	1%	5%
LB	80%	80%
UB	120%	120%

This study utilizes two fidelity models. The highest fidelity model, a 26×26 HFGMC (High-Fidelity General Method of Cells), provides detailed micromechanical insights. The lower fidelity model, a 2×2 GMC (General Method of Cells), offers a computationally efficient alternative. Computational costs were averaged over 100 runs to quantify fidelity-specific resource demands. To ensure accuracy, the target root mean square error (RMSE) was constrained to 20% of the weighted sum of the initial samples' mean values. The combined mean squared error (MSE) target is expressed as:

$$J_{\text{tol}} = \boldsymbol{\delta}^T (0.2\hat{\boldsymbol{s}}_{n_init})^2,$$

Results and discussion

To evaluate the efficiency of MFMC in micromechanics uncertainty quantification, we analyzed fiber orientations for $\{0^\circ, 45^\circ, 90^\circ, 135^\circ\}$. For each orientation, we calculated the mean and variance of the constitutive tensor elements, incorporating input uncertainties with standard deviations of 1% and 5%. Table 4.3 summarizes these results.

Table 4.3. Constitutive tensor elements for different fiber angles (1% and 5% Standard Deviation). Standard deviation results are given as a percentage of the mean.

Angle	Metric	C_{11}	C_{12}	C_{13}	C_{22}	C_{23}	C_{33}
0°	**Mean**	154910	2838	0	9627	0	4885
	$\sigma_{1\%}$	1	0.38	0	0.34	0	0.73
	$\sigma_{5\%}$	4.96	1.95	0	1.75	0	3.74
45°	**Mean**	47406	37636	-36286	47406	-36286	39680
	$\sigma_{1\%}$	0.73	0.95	0.97	0.73	0.97	0.89
	$\sigma_{5\%}$	4.08	5.11	5.29	4.08	5.29	4.83
90°	**Mean**	9628	2846	0	154920	0	4885
	$\sigma_{1\%}$	0.34	0.36	0	1	0	0.73
	$\sigma_{5\%}$	1.75	1.84	0	4.96	0	3.74
135°	**Mean**	47406	37636	36286	47406	36286	39680
	$\sigma_{1\%}$	0.73	0.95	0.97	0.73	0.97	0.89
	$\sigma_{5\%}$	4.08	5.11	5.29	4.08	5.29	4.83

In Table 4.3, the mean values align with the expected fourth-order tensor rotation behavior described by equation (2.11). In contrast, variances exhibit nonlinear behavior, necessitating the recalculation of statistical moments for each angle in the robust optimization loop. Notably, at 0° and 90°, out-of-plane shear-traction coupling elements are zero, consistent with theoretical expectations.

Next, we next compare the efficiency of MFMC versus MC in terms of speedup while maintaining an error bound. For each fiber angle, we calculate the number of high-fidelity samples required to reach the target MSE with both MC and MFMC. The speedup achieved by MFMC is determined by dividing the MC sample count by the MFMC sample count, and we report the sample allocations for each fidelity level.

Table 4.4. MFMC Speedup and Sampling for 1% STD

Angle	0°	45°	90°	135°
MC equivalent HF Samples	843	221	843	221
MFMC equivalent HF Samples	23	21	23	21
Speedup using MFMC	**36**	**11**	**36**	**11**
HFGMC Samples	20	20	20	20
GMC Samples	856	255	862	255

The equivalent high-fidelity samples represent the required high-fidelity model samples to achieve the target MSE. For MC, this is calculated by dividing the mean and auxiliary variable variances by the target MSE according to equation

$$J_{\text{tol}} = \frac{\sigma_1^2 + \tau_1^2}{m_1}.$$

In the MFMC case, the equation includes contributions from lower-fidelity models, as outlined in equation (2.46). The speedup is calculated by dividing the "MC Equivalent HF Samples" by the "MFMC Equivalent HF Samples", with the highest speedup observed at 0°

and 90° angles. This variation in speedup across angles highlights the effects of tensor rotation, which introduces nonlinear scaling in the MSE.

Increasing input variance to 5 % further amplifies the speedup, as shown in Table 4.5. This is due to higher model evaluation requirements under increased uncertainty, which favor the computational efficiency of the lower-fidelity model. In cases where the correlation coefficient approaches one, nearly all samples are allocated to the lower-fidelity model, approaching the theoretical speedup limit.

Table 4.5. Summary of MFMC Speedup and Sample Allocations for Micromechanics with 5% STD.

Metric	**0°**	**45°**	**90°**	**135°**
MC HF Samples	21081	5504	21080	5504
MFMC equivalent HF Samples	100	42	100	42
Speedup using MFMC	210	128	210	128
HFGMC Samples	20	20	20	20
GMC Samples	21268	6060	21277	6060

Tables 4.4 and 4.5 show that MFMC allocate nearly all samples to the lower-fidelity model due to high correlation and significant CPU time savings, providing a substantial speedup. This trend is observed when the correlation coefficient approaches one and lower fidelity models are significantly faster, approaching the theoretical speedup limit. To illustrate this, let's consider the case of one mechanical property for simplicity.

Remark 1. *Assume a bi-fidelity problem where the correlation coefficient for the QoI and the auxiliary variable is* $\rho_{1,2}$, $q_{1,2} \to 1-\varepsilon$ *and* $\varepsilon \to 0$. *The optimal sampling ratio, Equation* (2.41), *becomes*

$$r_2^* = \sqrt{\frac{w_1}{w_2}}\varepsilon^{-1/2}.$$

This means that as ε *approaches zero, the sampling becomes an MC analysis over the second fidelity model. We can also assess this statement through the MSE expression. Equations* (2.46) *and* (2.43) *can be combined to form the following expression:*

$$J_{tol} = \frac{1}{m_1^*}\frac{\sigma_1^2 + \xi\tau_1^2}{r_2^*} = \frac{\sigma_1^2 + \xi\tau_1^2}{m_2^*},$$

which is the expression for an MC simulation only using the second fidelity model. Therefore, if the correlation of a cheaper-to-evaluate model is very close to one, the algorithm chooses to evaluate that model all the time, and the method reduces to MC simulation of the lower fidelity model while satisfying the MSE error constraint for the highest fidelity.

Remark 1 illustrates that while the MFMC algorithm prioritizes lower-fidelity models under high correlation, high-fidelity models remain critical to address bias. For example, Table 4.1 highlights a significant difference in property G_{12} between the HFGMC and GMC models, with a relative error of approximately 7.3%. In micromechanics problems involving more complex fiber arrangements, such as hexagonal or random packing, this bias can exceed 28% [2]. Thus, high-fidelity models are indispensable for ensuring accuracy in uncertainty quantification frameworks.

Table 4.6. Comparison of GMC values to HFGMC

	C_{11}	C_{12}	C_{22}	C_{33}
HFGMC	154962	2837.5	9626.8	4884.3
GMC	154909	2762.7	9413.9	4529.0
Relative error (%)	0.03	2.64	2.21	7.27

Validation is performed in two stages: the estimation of mean values and the estimation of variances to ensure the validity of the modifications and implementation of the MFMC method. For a linear or quasi-linear problem, such as the homogenization problem studied here, inputs sampled from Gaussian distributions result in Gaussian-distributed outputs. The output mean corresponds to the model evaluated with the mean inputs [31]. This property allows us to validate both MC and MFMC analyses by comparing their mean estimates with the deterministic results obtained using nominal inputs. The estimates must lie within 3 RMSEs of the deterministic values for the results to be considered valid.

To evaluate this criterion, we define the RMSE distance. This distance is the absolute value of the difference between the estimator value (MC or MFMC) and the reference value (deterministic case), normalized by the estimator's RMSE:

$$d_{RMSE} = \frac{|\text{value}_{\text{estimator}} - \text{value}_{\text{ref}}|}{\text{RMSE}} \tag{4.1}$$

Table 4.7 presents the mean values of the mechanical properties estimated by deterministic analysis, MC, and MFMC, along with the RMSEs and RMSE distances. The deterministic results are obtained using mean input values and the HFGMC theory, while MC and MFMC use stochastic inputs, with MFMC incorporating both HFGMC (high fidelity) and GMC (low fidelity) models.

Table 4.7. Mean values of mechanical properties for deterministic case, MC analysis, and MFMC analysis. RMSEs of MC and MFMC estimators and their distance to the deterministic case proportional to their RMSE. Units are in MPa.

	C_{11}	C_{12}	C_{22}	C_{33}
Deterministic	154962	2837.5	9626.8	4884.3
MC	154910	2837.6	9626.9	4884.5
MFMC	154910	2837.7	9627.2	4883.8
RMSE MC	19.79	0.17	0.50	0.55
d_{RMSE}^{MC}	2.65	0.60	0.20	0.37
RMSE MFMC	19.69	0.18	0.52	0.57
d_{RMSE}^{MFMC}	2.66	1.09	0.78	0.87

The results indicate that for all mechanical properties, both MC and MFMC estimates are within 3 RMSEs of the deterministic values, satisfying the validation criterion for mean estimation. This confirms the correct implementation of MC and the successful formulation and application of MFMC for estimating mean values.

Having validated the MC analysis, we use its variance results as a reference to validate the MFMC variance calculations. Variance estimates are less predictable than mean estimates, and the RMSE distances can exceed 3 due to the inherent uncertainty in both MC and MFMC estimates. Table 4.8 compares variance estimates from MC and MFMC and their relative RMSE distances.

Table 4.8. MC and MFMC variance estimations, MFMC RMSE for the variance, and relative RMSE distance between MC and MFMC estimations.

	MC	**MFMC**	**RMSE MFMC**	**MFMC Distance to Nominal**
$\boldsymbol{C}_{11}$	2340000	2281500	40294	1.45
$\boldsymbol{C}_{12}$	119.7	121.3	3.14	0.49
$\boldsymbol{C}_{22}$	1108.3	1121.7	23.65	0.57
$\boldsymbol{C}_{33}$	1301.3	1322.1	31.65	0.66

The variance estimates from MC and MFMC are within three RMSE of each other, indicating the correctness of the MFMC method for variance estimation in micromechanical uncertainty quantification.

In conclusion, the MFMC method demonstrates substantial computational efficiency gains over MC for micromechanics under uncertainty, particularly when input variance is high. The variation in speedup based on fiber angle suggests that the constitutive tensor's rotational properties introduce nonlineary in the MSE computation, making MFMC advantageous in robust optimization involving complex material orientations.

The MFMC method significantly improves computational efficiency over MC, particularly for problems involving high input variance. The variation in speedup across fiber angles reflects the influence of constitutive tensor rotation, which introduces nonlinear scaling in the MSE.

While the algorithm prioritizes lower-fidelity models when correlation coefficients are high, the inclusion of high-fidelity models remains critical to address potential biases. For example, as shown in Table 4.1, the relative error between HFGMC and GMC results for C_{33} is approximately 7.3%, and this error can be significantly higher for more complex fiber arrangements [2]. Thus, high-fidelity models are essential for ensuring accuracy in uncertainty quantification frameworks.

The validation of the MFMC method confirms its ability to reliably estimate both mean and variance of mechanical properties while achieving significant computational speedup. This makes it a powerful tool for robust optimization and uncertainty quantification in micromechanics, particularly for composite materials with complex material orientations and high input variability.

4.2 Multiscale robust topology optimization of MBB beam

The second example involves an MBB beam with a single domain. The objective is to validate the multiscale multifidelity robust topology optimization (mfRTO) method for unidirectional composite materials. Specifically, we compare deterministic and robust analyses of the MBB beam to demonstrate that even for mean minimization ($\eta = 1$), the variance of the robust solution is reduced compared to the deterministic case. Additionally, this example validates the calculation of mean and variance during each topology optimization iteration, as well as the correctness of the overall optimization process. Lastly, we compare the computational efficiency (speedup) of mfRTO with a robust topology optimization (RTO) method using a standard Monte Carlo approach.

Problem Definition

The geometry of the MBB beam is 240×40, with the left side simply supported and the right side resting on a roller. A load is applied at the midpoint of the top edge.

For each finite element, the constitutive tensor elements are sampled using the online approach described in Section 4.1. The target mean square error (MSE) is set to 2% of the mean compliance. Fidelity levels are defined based on mesh resolution and the order of shape functions, maintaining a 6:1 ratio between the number of elements in x and y directions. Table 4.9 outlines the mesh resolution for each fidelity model, while Figure 4.1 illustrates the geometry and boundary conditions.

Table 4.9. Mesh resolution and shape function order for each fidelity model.

	$\mathbb{F}_1$	$\mathbb{F}_2$	$\mathbb{F}_3$	$\mathbb{F}_4$
Mesh Size	40×240	40×240	20×120	10×60
Shape Function Order	2	1	1	1

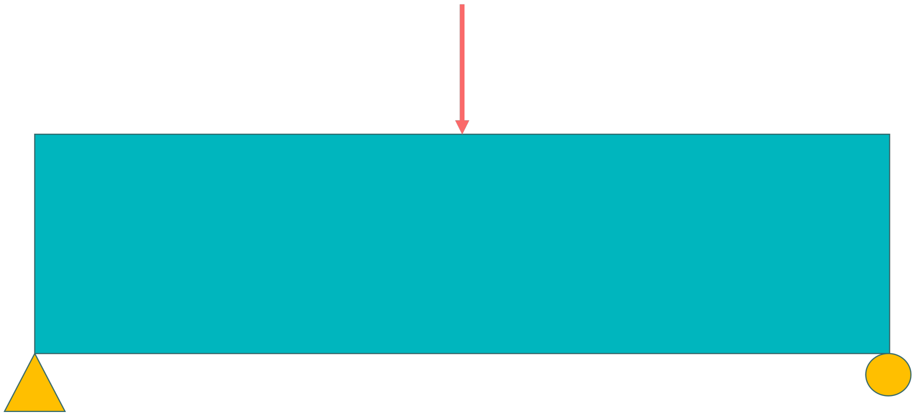

Figure 4.1. MBB beam geometry and boundary conditions.

Implementation

In the MBB problem, incorporating online material property evaluation significantly impacts the required computational budget compared to using precomputed homogenized properties and performing the rotation over the sampled properties. The precomputed approach achieves correlation coefficients above 99% for both the quantity of interest (QoI) and the auxiliary variable across all fidelity models. In contrast, the online approach exhibits lower correlation coefficients in the first iteration, with approximately 0.8 for the QoI and 0.6 for the auxiliary variable.

The reduced correlation impacts the sampling strategy, as fewer samples are allocated to lower-fidelity models equation (2.41), necessitating a higher overall computational budget to meet the user-defined MSE, equation (2.46). Furthermore, the higher nonlinearity in the constitutive tensor variance during the online approach, equation (3.2), demands additional initial samples to accurately estimate compliance variance (σ_1 and τ_1). Insufficient sampling may result in non-converged estimates for the mean and variance and potential failure of the algorithm due to the control variate coefficient (β) driving variance estimates to negative values.

Results and discussion

The first step in this analysis is to compare the deterministic topology optimization approach to the robust one. For this comparison, we focus on mean compliance minimization by setting $\eta = 1$. Despite this simplification, we expect the robust approach to yield designs with improved robustness compared to the deterministic case.

Figure 4.2 compares the final topologies for the deterministic and robust cases. While the overall designs appear similar, there are key differences. The deterministic case lacks certain members that appear in the robust design, even though they are discontinuous in appearance. This discontinuity is an artifact of visualization; the level-set function inherently prevents these cuts. Another noticeable difference is the thicker central triangle in the robust design compared to the deterministic one. This suggests that, for composite materials, robustness is achieved by increasing member thickness rather than introducing additional members, as is often the case with isotropic materials.

(a) Deterministic case.

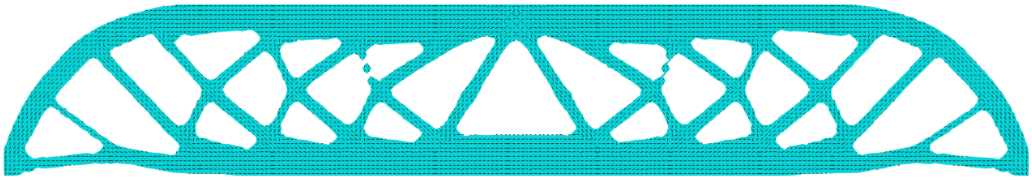

(b) Robust case with multi-fidelity.

Figure 4.2. Final MBB beam topology for deterministic and robust cases.

The optimization histories of the deterministic and robust cases are shown in Figure 4.3. Both cases exhibit similar convergence trends, with some notable differences. The deterministic case begins with a higher compliance value and converges to a final value approximately 4% lower than the robust case. This indicates that the robust case may converge to a local minimum when optimizing solely for compliance. However, this drawback is offset by the robust case's significant reduction in standard deviation, leading to a more reliable design under uncertainty.

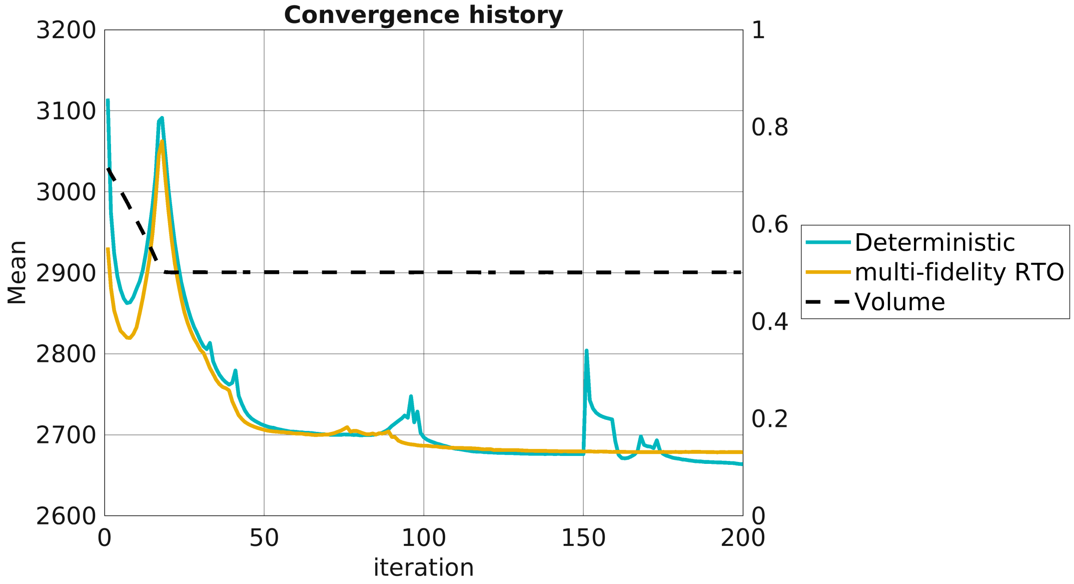

Figure 4.3. Convergence history comparison for MBB deterministic case.

To evaluate the effectiveness of the robust analysis compared to the deterministic approach, we conducted a Monte Carlo (MC) analysis using 5,000 samples for the final topology in both cases. Figure 4.4 shows the resulting compliance distributions. For the robust case (Figure 4.4b), the compliance mean is approximately 15 points higher than the deterministic case (Figure 4.4a). However, the yellow lines on the edges, representing two standard deviations, are much closer to the mean for the robust case, 20 points compared to 35 points for the deterministic case, indicating a significant reduction in variability.

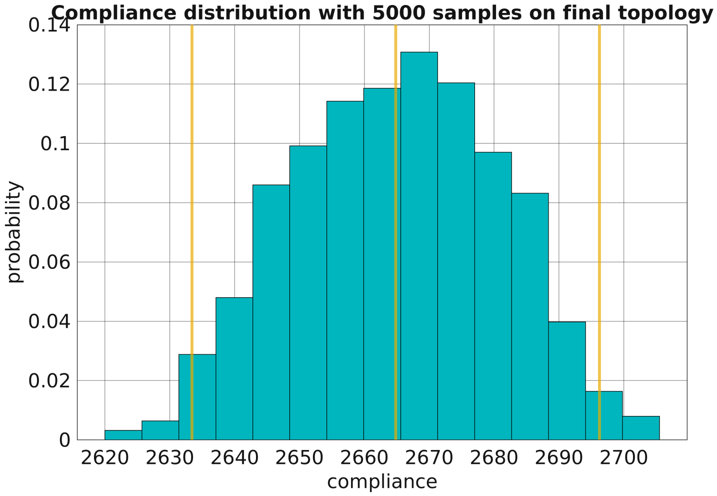

(a) Deterministic case.

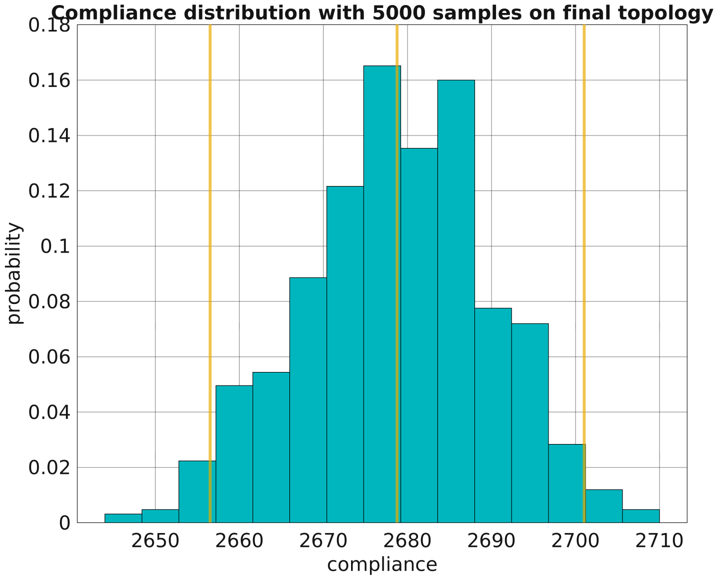

(b) Robust case with multi-fidelity.

Figure 4.4. Compliance histograms for deterministic and robust cases over 5,000 Monte Carlo samples. The edge yellow lines represent ±2 standard deviations.

To further quantify these observations, Table 4.10 compares the exact mean and standard deviation values. While the robust case exhibits a slight 3.92% increase in compliance mean relative to the deterministic case, it achieves a 41.4% reduction in standard deviation. These results underscore the effectiveness of robust topology optimization in reducing variability and ensuring more reliable performance under uncertainty.

Table 4.10. Comparison of mean and standard deviation values for deterministic and robust topology optimization.

	Deterministic	**MFMC Robust**	**Difference**
Mean	2665	2679	+3.92%
Standard Deviation	15.7	11.1	-41.4%

These findings proof that the robust topology optimization approach, even when focused solely on mean compliance minimization, offers substantial improvements in reliability by reducing variability, highlighting its advantage over deterministic designs in uncertain environments.

To validate the correctness of the multi-fidelity robust topology optimization (mfRTO) framework, we compare its results to those obtained from a single-fidelity Monte Carlo (MC) RTO analysis. This validation aims to ensure the accuracy of both the optimization process and the mean and variance estimations provided by the MFMC framework.

The final topologies obtained using mfRTO and single-fidelity RTO are compared in Figure 4.5. The results show that the two methods yield identical topologies, confirming that the optimization process in the mfRTO framework accurately replicates the single-fidelity RTO results.

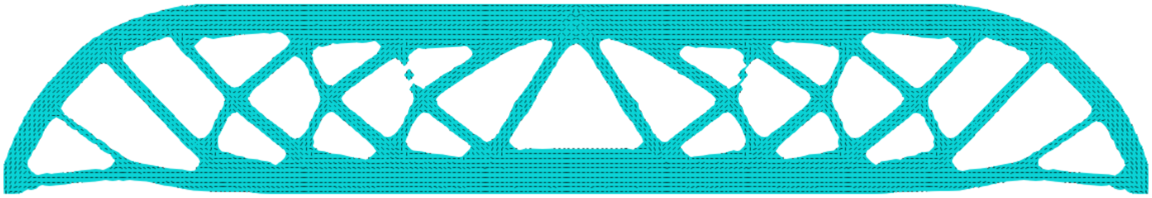

(a) mfRTO case.

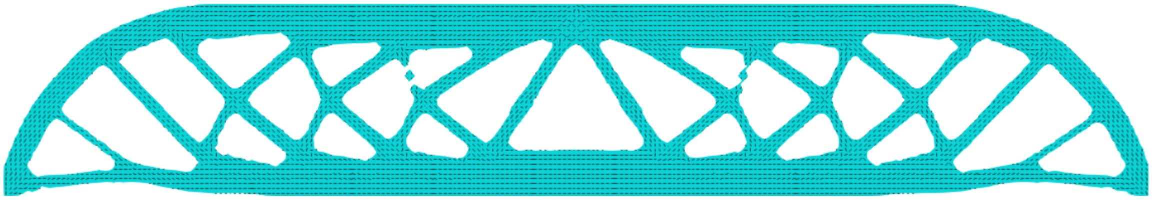

(b) RTO case.

Figure 4.5. mfRTO VS RTO comparison for MBB example

To further validate the optimization process, we evaluate the mean and variance of compliance over the iterations for both approaches. Figure 4.6 shows that the mean and variance evolution graphs for mfRTO and single-fidelity RTO overlap, confirming consistency between the methods. Table 4.11 compares the final values of mean and standard deviation, showing negligible differences ($< 0.1\%$ for mean and $< 0.01\%$ for standard deviation).

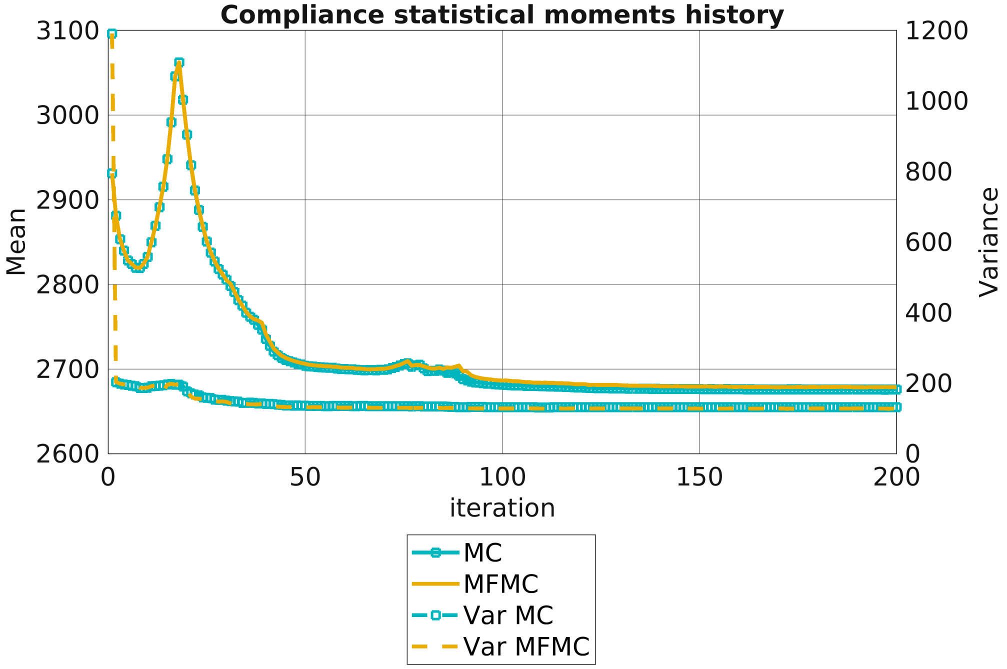

Figure 4.6. Mean and variance over the optimization process for MC and MFMC appraoches.

Table 4.11. Comparison between mean and standard deviation values for multi-fidelity RTO VS single fidelity RTO from the optimization process

	MFMC Robust	**MC Robust**	**Difference**
Mean	2678.5	2676	0.09%
Standard deviation	11.5	11.5	$< 0.01\%$

These results confirm the correctness of the optimization process in the mfRTO framework. The final step is to validate the accuracy of mean and variance calculations at each iteration. To achieve this, we analyze the final topology using a Monte Carlo (MC) analysis with 5,000 samples and compute the mean and variance for the MFMC approach. The values obtained are then compared with those estimated by the optimizer at the end of the optimization process to quantify the differences between the MC and MFMC estimators.

Table 4.12 summarizes the results. The mean compliance values from both methods are nearly identical, with a difference of only 0.011 %. The standard deviation values also agree closely, with a slightly larger difference of 3.60 %, which is within 3 RMSEs. These minimal discrepancies confirm the reliability and accuracy of the MFMC framework in estimating mean and variance during the optimization process.

Table 4.12. Comparison between mean and standard deviation values for multi-fidelity RTO VS single fidelity RTO over final topology using a 5000 samples MC analysis

	MFMC	**MC**	**Difference**
Mean	2678.5	2678.8	0.011%
Standard deviation	11.5	11.1	3.60%

The speedup of this calculation is summarized in figure 4.7, where the peak speedup over an iteration is 1.87 times faster than MC analysis. The average speedup is 1.42 times faster than MC analysis, which means we save almost 50 % of the computation time even when the computational cost of the highest fidelity barely surpasses 1 second. For models where the computational cost ratio is higher the speedup can be greatly enhanced as shown in [30]. This cumulative speedup or average speedup is computed by the ratio between the total number, over all the iterations, of equivalent high-fidelity samples of MFMC to high-fidelity samples of MC. Hence, we have proven the effectiveness of the method for multiscale robust topology optimization.

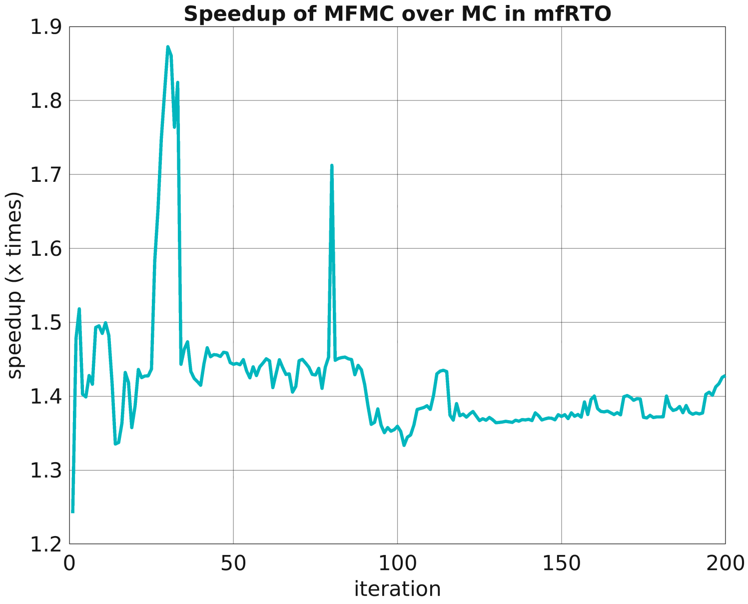

Figure 4.7. MFMC speedup over MC for each topology optimization iteration.

From the MBB beam example, the following conclusions can be drawn: the mfRTO framework produces results that are virtually identical to those of single-fidelity RTO, both in terms of topology and optimization metrics. This validates the robustness and reliability of the multi-fidelity approach. The multi-fidelity framework demonstrates a significant computational advantage over single-fidelity RTO by leveraging lower-fidelity models while maintaining accuracy. This efficiency makes it suitable for large-scale robust optimization problems. Comparing the final topology with 5,000 Monte Carlo samples confirms the consistency of the mfRTO framework's estimators. Differences between the MFMC and MC results for mean compliance (0.011%) and standard deviation (3.6%) are within the expected error range, validating the accuracy of the multi-fidelity estimators. The robust design reduces variability in compliance while achieving comparable mean compliance to the deterministic design. This demonstrates the effectiveness of robust topology optimization in delivering more reliable and predictable designs under uncertainty.

Overall, the MBB beam example showcases that the mfRTO framework is both accurate and computationally efficient, providing a strong foundation for robust optimization in complex engineering applications.

Chapter 4, in part is currently being prepared for submission for publication of the material. Diaz-Flores Caminero, Alvaro; Ismail, Hussein; Chadhuri, Anirban; Kim, H. Alicia. The thesis author was the primary investigator and author of this material.

Chapter 5

Conclusions and future work

5.1 Conclusion

In this thesis, we enhanced the multi-fidelity Monte Carlo (MFMC) method to handle multiple quantities of interest, enabling uncertainty quantification in homogenization problems. The method's performance was demonstrated using the High-Fidelity General Method of Cells (HFGMC) and the General Method of Cells (GMC) with varying Repetitive Unit Cell discretizations, achieving over 200-fold speedup. We investigated the influence of input variance on speedup and validated the framework and results through comparison with a Monte Carlo analysis comprising 5,000 evaluations using HFGMC theory.

Additionally, we formulated a multiscale robust topology optimization problem for distributing composite materials within the design domain while optimizing fiber orientation to minimize strain energy. Customized angle sets were analyzed and compared to analytical solutions to showcase the approach's effectiveness.

Furthermore, the multiscale robust topology optimization framework was reformulated to account for anisotropic material uncertainty, demonstrating variance reduction compared to the deterministic approach. The updated method achieved a 1.42-fold speedup over the Monte Carlo approach.

5.2 Future work

This work establishes a robust framework for multiscale optimization under uncertainty; however, several avenues for further research could extend and refine its capabilities.

At the material level, potential improvements include optimizing the distribution of fibers and matrix at the constituents level to achieve better performance. Exploring optimal stacking sequences for layered composites could also enhance material properties and design efficiency.

From a macroscale perspective, incorporating additional objectives such as minimizing strain energy under stress constraints, performing thermo-mechanical analysis, or accounting for nonlinear material behavior would add complexity and realism to the finite element analysis.

Lastly, comparing the computational results with experimental data would provide a critical validation step, ensuring the framework's applicability and accuracy in real-world scenarios. These extensions would collectively elevate the fidelity and utility of the proposed methods.

Chapter 5, in part is currently being prepared for submission for publication of the material. Diaz-Flores Caminero, Alvaro; Ismail, Hussein; Chadhuri, Anirban; Kim, H. Alicia. The thesis author was the primary investigator and author of this material.

Bibliography

[1] Jacob Aboudi. The generalized method of cells and high-fidelity generalized method of cells micromechanical models—a review. Mechanics of Advanced Materials and Structures, 11(4-5):329–366, 2004.

[2] Jacob Aboudi, Steven Arnold, and Brett Bednarcyk. 1 - introduction. In Jacob Aboudi, Steven Arnold, and Brett Bednarcyk, editors, Practical Micromechanics of Composite Materials, pages 1–19. Butterworth-Heinemann, 2021.

[3] Gourav Agrawal, Abhinav Gupta, Rajib Chowdhury, and Anupam Chakrabarti. Robust topology optimization of negative poisson's ratio metamaterials under material uncertainty. Finite Elements in Analysis and Design, 198:103649, 2022.

[4] Haichao An, Byeng D. Youn, and Heung Soo Kim. Variable-stiffness composite optimization using dynamic and exponential multi-fidelity surrogate models. International Journal of Mechanical Sciences, 257:108547, 2023.

[5] Erik Andreassen and Casper Schousboe Andreasen. How to determine composite material properties using numerical homogenization. Computational Materials Science, 83:488–495, 2014.

[6] Mahdi Arian Nik, Kazem Fayazbakhsh, Damiano Pasini, and Larry Lessard. Surrogate-based multi-objective optimization of a composite laminate with curvilinear fibers. Composite Structures, 94(8):2306–2313, 2012.

[7] Martin Philip Bendsøe and Noboru Kikuchi. Generating optimal topologies in structural design using a homogenization method. Computer Methods in Applied Mechanics and Engineering, 71(2):197–224, 1988.

[8] Narasimha Boddeti, Yunlong Tang, Kurt Maute, David W. Rosen, and Martin L. Dunn. Optimal design and manufacture of variable stiffness laminated continuous fiber reinforced composites. Scientific Reports, 2020.

[9] Walter L. Bond. The mathematics of the physical properties of crystals. The Bell System Technical Journal, 22(1):1–72, 1943.

[10] Matteo Bruggi, Hussein Ismail, and János Lógó. Topology optimization with graded infill accounting for loading uncertainty. Composite Structures, 311:116807, 2023.

[11] Matteo Bruggi, Gabriele Milani, and Alberto Taliercio. Design of the optimal fiber-reinforcement for masonry structures via topology optimization. International Journal of Solids and Structures, 50(13):2087–2106, 2013.

[12] Jinhu Cai, Long Huang, Hongyu Wu, and Lairong Yin. Concurrent topology optimization of multiscale structure under uncertain dynamic loads. International Journal of Mechanical Sciences, 251:108355, 2023.

[13] Jinhu Cai, Chunjie Wang, and Zhifang Fu. Robust concurrent topology optimization of multiscale structure under single or multiple uncertain load cases. International Journal for Numerical Methods in Engineering, 121(7):1456–1483, 2020.

[14] Anirban Chaudhuri, John Jasa, Joaquim RRA Martins, and Karen E Willcox. Multifidelity optimization under uncertainty for a tailless aircraft. In 2018 AIAA Non-Deterministic Approaches Conference, page 1658, 2018.

[15] H. C. Cheng, N. Kikuchi, and Z. D. Ma. An improved approach for determining the optimal orientation of orthotropic material. Structural optimization, 8:101–112, 1994.

[16] Sheng Chu, Mi Xiao, Liang Gao, Yan Zhang, and Jinhao Zhang. Robust topology optimization for fiber-reinforced composite structures under loading uncertainty. Computer Methods in Applied Mechanics and Engineering, 384:113935, 2021.

[17] Andre Luis Ferreira da Silva, Ruben Andres Salas, Emilio Carlos Nelli Silva, and JN Reddy. Topology optimization of fibers orientation in hyperelastic composite material. Composite Structures, 231:111488, 2020.

[18] Jiadong Deng and Wei Chen. Concurrent topology optimization of multiscale structures with multiple porous materials under random field loading uncertainty. Structural and Multidisciplinary Optimization, 56:1–19, 2017.

[19] Akshay Desai, Mihir Mogra, Gundavarapu Sesha, Kiran Kumar, Gundavarapu Sesha, and G. K. Ananthasuresh. Topological-derivative-based design of stiff fiber-reinforced structures with optimally oriented continuous fibers. Structural and Multidisciplinary Optimization, 63:703–720, 2021.

[20] Peter Dunning, Alicia Kim, and Glen Mullineux. Introducing uncertainty in direction of loading for topology optimization. In 51st Structures, Structural Dynamics, and Materials Conference, 2010.

[21] Peter D. Dunning, H. Alicia Kim, and Glen Mullineux. Introducing loading uncertainty in topology optimization. AIAA Journal, 49(4):760–768, 2011.

[22] Rossana R. Fernandes, Nekoda van de Werken, Pratik Koirala, Timothy Yap, Ali Y. Tamijani, and Mehran Tehrani. Experimental investigation of additively manufactured continuous fiber reinforced composite parts with optimized topology and fiber paths. Additive Manufacturing, 44:102056, 2021.

[23] Yogesh Gandhi and Giangiacomo Minak. A review on topology optimization strategies for additively manufactured continuous fiber-reinforced composite structures. Applied Sciences, 12(21), 2022.

[24] H.C. Gea and J. H. Luo. On the stress-based and strain-based methods for predicting optimal orientation of orthotropic materials. Structural and Multidisciplinary Optimization, 26(3):229,234, 2004.

[25] L. V. Gibiansky and A. V. Cherkaev. Microstructures of Composites of Extremal Rigidity and Exact Bounds on the Associated Energy Density, pages 273–317. Birkhäuser Boston, 1997.

[26] Jeroen P. Groen and Ole Sigmund. Homogenization-based topology optimization for high-resolution manufacturable microstructures. International Journal for Numerical Methods in Engineering, 113(8):1148–1163, 2018.

[27] JoséMiranda Guedes and Noboru Kikuchi. Preprocessing and postprocessing for materials based on the homogenization method with adaptive finite element methods. Computer Methods in Applied Mechanics and Engineering, 83(2):143–198, 1990.

[28] Khader M. Hamdia, Hamid Ghasemi, Xiaoying Zhuang, and Timon Rabczuk. Multilevel monte carlo method for topology optimization of flexoelectric composites with uncertain material properties. Engineering Analysis with Boundary Elements, 134:412–418, 2022.

[29] Tim Heitkamp, Sebastian Kuschmitz, Simon Girnth, Justin-Dean Marx, Günter Klawitter, Nils Waldt, and Thomas Vietor. Stress-adapted fiber orientation along the principal stress directions for continuous fiber-reinforced material extrusion. Progress in Additive Manufacturing, 8(3):541–559, June 2023.

[30] Jaeyub Hyun, Anirban Chaudhuri, Karen E Willcox, and Hyunsun A Kim. Multifidelity robust topology optimization for material uncertainties with digital manufacturing. In AIAA SCITECH 2023 Forum, page 2038, 2023.

[31] Frederick James. Monte carlo theory and practice. Reports on progress in Physics, 43(9):1145, 1980.

[32] Dustin R. Jantos, Klaus Hackl, and Philipp Junker. Topology optimization with anisotropic materials, including a filter to smooth fiber pathways. Structural and Multidisciplinary Optimization, 61:2135–2154, 2020.

[33] Ghais Kharmanda, N. Olhoff, Alaa Mohamed, and M. Lemaire. Reliability-based topology optimization. Structural and Multidisciplinary Optimization, 26:295–307, 03 2004.

[34] V Kouznetsova, M G D Geers, and W A M Brekelmans. Multi-scale constitutive modelling of heterogeneous materials with a gradient-enhanced computational homogenization scheme. Int. J. Numer. Methods Eng., 54(8):1235–1260, July 2002.

[35] Dinesh Kumar, Yao Koutsawa, Gaston Rauchs, Mariapia Marchi, Carlos Kavka, and Salim Belouettar. Efficient uncertainty quantification and management in the early stage design of composite applications. Composite Structures, 251:112538, 2020.

[36] Dinesh Kumar, Mariapia Marchi, Syed Bahauddin Alam, Carlos Kavka, Yao Koutsawa, Gaston Rauchs, and Salim Belouettar. Multi-criteria decision making under uncertainties in composite materials selection and design. Composite Structures, 279:114680, 2022.

[37] Hang Li, Liang Gao, Hao Li, Xiaopeng Li, and Haifeng Tong. Full-scale topology optimization for fiber-reinforced structures with continuous fiber paths. Computer Methods in Applied Mechanics and Engineering, 377:113668, 2021.

[38] Zeshang Li, Lei Wang, and Geng Xinyu. A level set reliability-based topology optimization (ls-rbto) method considering sensitivity mapping and multi-source interval uncertainties. Computer Methods in Applied Mechanics and Engineering, 419:116587, 2024.

[39] A.V. Malakhov and A.N. Polilov. Design of composite structures reinforced curvilinear fibres using fem. Composites Part A: Applied Science and Manufacturing, 87:23–28, 2016.

[40] Andreas Neofytou, Thiago Rios, Mariusz Bujny, Stefan Menzel, and H. Alicia Kim. Level set topology optimization with sparse automatic differentiation. Structural and Multidisciplinary Optimization, 67(10):178, 2024.

[41] G. Papanicolau, A. Bensoussan, and J.L. Lions. Asymptotic Analysis for Periodic Structures. Elsevier Science, 1978.

[42] P. Pedersen. On optimal orientation of orthotropic materials. Structural Optimization, 1(2):101,106, 1989.

[43] Benjamin Peherstorfer, Karen Willcox, and Max Gunzburger. Optimal model management for multifidelity monte carlo estimation. SIAM Journal on Scientific Computing, 38(5):A3163–A3194, 2016.

[44] Zheng Qiu, Quhao Li, and Shutian Liu. Topology optimization method for continuous fiber reinforced composites with different moduli in tension and compression. Computer Methods in Applied Mechanics and Engineering, 423:116867, 2024.

[45] G.I. Schuëller and H.A. Jensen. Computational methods in optimization considering uncertainties – an overview. Computer Methods in Applied Mechanics and Engineering, 198(1):2–13, 2008. Computational Methods in Optimization Considering Uncertainties.

[46] Kentaro Sugiyama, Ryosuke Matsuzaki, Andrei V. Malakhov, Alexander N. Polilov, Masahito Ueda, Akira Todoroki, and Yoshiyasu Hirano. 3d printing of optimized composites with variable fiber volume fraction and stiffness using continuous fiber. Composites Science and Technology, 186:107905, 2020.

[47] Katsuyuki Suzuki and Noboru Kikuchi. A homogenization method for shape and topology optimization. Computer Methods in Applied Mechanics and Engineering, 93(3):291–318, 1991.

[48] Piotr Tauzowski, Bartłomiej Błachowski, and János Lógó. Optimal topologies considering fatigue with reliability constraint. Advances in Engineering Software, 189:103590, 2024.

[49] Dilaksan Thillaithevan, Paul Bruce, and Matthew Santer. Robust multiscale optimization accounting for spatially-varying material uncertainties. Struct. Multidiscipl. Optim., 65(2), February 2022.

[50] Mazdak Tootkaboni, Alireza Asadpoure, and James K Guest. Topology optimization of continuum structures under uncertainty–a polynomial chaos approach. Computer Methods in Applied Mechanics and Engineering, 201:263–275, 2012.

[51] Lei Wang, Bowen Ni, Xiaojun Wang, and Zeshang Li. Reliability-based topology optimization for heterogeneous composite structures under interval and convex mixed uncertainties. Applied Mathematical Modelling, 99:628–652, 2021.

[52] Ting Wang, Nanya Li, Guido Link, John Jelonnek, Jürgen Fleischer, Jörg Dittus, and Daniel Kupzik. Load-dependent path planning method for 3d printing of continuous fiber reinforced plastics. Composites Part A: Applied Science and Manufacturing, 140:106181, 2021.

[53] Xuan Wang, Zeng Meng, Bo Yang, Changzheng Cheng, Kai Long, and Jingchuan Li. Reliability-based design optimization of material orientation and structural topology of fiber-reinforced composite structures under load uncertainty. Composite Structures, 291:115537, 2022.

[54] Jun Wu, Ole Sigmund, and Jeroen P. Groen. Topology optimization of multi-scale structures: a review. Structural and Multidisciplinary Optimization, 63:1455 – 1480, 2021.

[55] Yanan Xu, Yunkai Gao, Chi Wu, Jianguang Fang, and Qing Li. Robust topology optimization for multiple fiber-reinforced plastic (frp) composites under loading uncertainties. Structural and Multidisciplinary Optimization, 59:695–711, 2019.

[56] Jin Zhang, Wei-Hong Zhang, and Ji-Hong Zhu. An extended stress-based method for orientation angle optimization of laminated composite. Acta Mechanica Sinica, 2011.

[57] Yongfeng Zheng, Zihao Chen, Baoshou Liu, Ping Li, Jiale Huang, Zhipeng Chen, and Jianhua Xiang. Robust topology optimization for multi-material structures considering material uncertainties. Thin-Walled Structures, 201:111990, 2024.